

AFRL-SN-RS-TR-2002-214
Final Technical Report
August 2002



SEMICONDUCTOR PHOTONIC COMPONENTS FOR RF APPLICATIONS

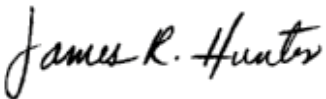
University of California, San Diego

APPROVED FOR PUBLIC RELEASE; DISTRIBUTION UNLIMITED.

**AIR FORCE RESEARCH LABORATORY
SENSORS DIRECTORATE
ROME RESEARCH SITE
ROME, NEW YORK**

This report has been reviewed by the Air Force Research Laboratory, Information Directorate, Public Affairs Office (IFOIPA) and is releasable to the National Technical Information Service (NTIS). At NTIS it will be releasable to the general public, including foreign nations.

AFRL-SN-RS-TR-2002-214 has been reviewed and is approved for publication.

APPROVED: 
JAMES R. HUNTER
Project Engineer

FOR THE DIRECTOR: 
RICHARD G. SHAUGHNESSY, Lt. Col., USAF
Chief, Rome Operations Office
Sensors Directorate

REPORT DOCUMENTATION PAGE

Form Approved
OMB No. 074-0188

Public reporting burden for this collection of information is estimated to average 1 hour per response, including the time for reviewing instructions, searching existing data sources, gathering and maintaining the data needed, and completing and reviewing this collection of information. Send comments regarding this burden estimate or any other aspect of this collection of information, including suggestions for reducing this burden to Washington Headquarters Services, Directorate for Information Operations and Reports, 1215 Jefferson Davis Highway, Suite 1204, Arlington, VA 22202-4302, and to the Office of Management and Budget, Paperwork Reduction Project (0704-0188), Washington, DC 20503

1. AGENCY USE ONLY (Leave blank)		2. REPORT DATE AUGUST 2002	3. REPORT TYPE AND DATES COVERED Final Mar 01 – Dec 01	
4. TITLE AND SUBTITLE SEMICONDUCTOR PHOTONIC COMPONENTS FOR RF APPLICATIONS			5. FUNDING NUMBERS C - F30602-01-2-0516 PE - 62204F PR - 2002 TA - SN WU - 01	
6. AUTHOR(S) Paul K. L. Yu, Yang Wu, G. L. Li, Yuling Zhuang, Phil Mages, A. R. Clawson, and W. X. Chen				
7. PERFORMING ORGANIZATION NAME(S) AND ADDRESS(ES) University of California, San Diego Office of Contract and Grant Administration 9500 Gilman Drive, Mail Code 0934 La Jolla California 92093-0934			8. PERFORMING ORGANIZATION REPORT NUMBER N/A	
9. SPONSORING / MONITORING AGENCY NAME(S) AND ADDRESS(ES) Air Force Research Laboratory/SNDP 25 Electronic Parkway Rome New York 13441-4515			10. SPONSORING / MONITORING AGENCY REPORT NUMBER AFRL-SN-RS-TR-2002-214	
11. SUPPLEMENTARY NOTES AFRL Project Engineer: James R. Hunter/SNDP/(315) 330-7045/ James.Hunter@rl.af.mil				
12a. DISTRIBUTION / AVAILABILITY STATEMENT APPROVED FOR PUBLIC RELEASE; DISTRIBUTION UNLIMITED.				12b. DISTRIBUTION CODE
13. ABSTRACT (Maximum 200 Words) The objective of this program was to advance the performance of the semiconductor waveguide modulator in externally modulated RF fiber-optic links for space-based and airborne platforms such as true time delay beam formation and beam steering subsystem in phased array antennas. Device and material approaches were investigated to improve the modulator based on semiconductor structures for achieving high spur free dynamic range (SFDR) and high frequency operation. In these approaches, the semiconductor optical modulators were specifically designed to achieve high slope efficiency and high center frequency, while at the same time maintaining minimal generation of spurious signals. The fiber-optic links using these modulators are expected to satisfy the low noise figure, high center frequencies, low power requirements. A high performance electroabsorption modulator with more than 40 GHz bandwidth has been fabricated and evaluated. A new design was investigated for a quantum well modulator that includes an intra-barrier to enhance the power handling and slope efficiency. Both theory and experiment has beer carried out to demonstrate this concept.				
14. SUBJECT TERMS Semiconductor Electroabsorption Modulator, Optical Waveguide Modulator, Traveling Wave Optical Modulator			15. NUMBER OF PAGES 36	
			16. PRICE CODE	
17. SECURITY CLASSIFICATION OF REPORT UNCLASSIFIED	18. SECURITY CLASSIFICATION OF THIS PAGE UNCLASSIFIED	19. SECURITY CLASSIFICATION OF ABSTRACT UNCLASSIFIED	20. LIMITATION OF ABSTRACT UL	

TABLE OF CONTENTS

TECHNICAL OBJECTIVE:	1
SUMMARY OF ACCOMPLISHMENTS	1
DETAILED TECHNICAL ACHIEVEMENT ON EFFORT	2
1. WIDE BANDWIDTH TRAVELING-WAVE INGAASP/INP ELECTROABSORPTION MODULATOR: MEASUREMENT AND ANALYSIS	2
<i>Theory</i>	3
<i>Device Design</i>	5
<i>DC Characteristics</i>	6
<i>Microwave Properties</i>	7
<i>Modulation Frequency Response</i>	9
<i>Optical Saturation Power</i>	11
2. HIGH-POWER ELECTROABSORPTION MODULATOR USING INTRA-STEP-BARRIER QUANTUM WELLS	12
REFERENCES	19
PUBLICATIONS	20
THESES SUPPORTED BY THIS CONTRACT:	20
ACKNOWLEDGMENTS	20
APPENDIX A WIDE BANDWIDTH TRAVELING-WAVE INGAASP/INP ELECTROABSORPTION MODULATOR FOR MILLIMETER WAVE APPLICATIONS	21
APPENDIX B HIGH SATURATION, HIGH SPEED TRAVELING-WAVE INGAASP/INP ELECTROABSORPTION MODULATOR	25
APPENDIX C ANALYSIS OF INTRA-STEP-BARRIER QUANTUM WELLS FOR HIGH-POWER ELECTROABSORPTION MODULATORS	28

TABLE OF FIGURES

FIGURE 1	DISTRIBUTED CIRCUIT MODEL FOR TW-EAM TRANSMISSION LINE.....	4
FIGURE 2	NORMALIZED TRANSMISSION AND MODULATOR CURRENT VERSUS BIAS FOR A TW-EAM WITH 200 μm ACTIVE LENGTH PLUS 100 μm LONG PASSIVE WAVEGUIDE.	7
FIGURE 3	MICROWAVE ATTENUATION FACTOR AND PHASE VELOCITY INDEX OF TW-EAM WAVEGUIDE. SYMBOLS ARE VALUES EXTRACTED FROM MEASUREMENT; SOLID LINES ARE THE BEST-FIT USING THE CIRCUIT MODEL SHOWN IN FIG. 1.	8
FIGURE 4	WAVEGUIDE IMPEDANCE OF THE TW-EAM, CALCULATED USING THE EQUIVALENT CIRCUIT MODEL IN FIG. 1.	9
FIGURE 5	MEASURED (NOISY LINES) AND CALCULATED (SMOOTH LINES) FREQUENCY RESPONSE CURVES FOR TWO TW-EAM DEVICES. THE DETECTOR RESPONSIVITY IS ~ 0.12 A/W UP TO 40 GHz	10
FIGURE 6	HIGH-FREQUENCY OPTICAL SATURATION POWER FOR TWO 200 μm LONG TW-EAMS WITH 100 μm LONG PASSIVE LENGTH.....	11
FIGURE 7	IQWS AT DIFFERENT ELECTRIC FIELD (A) 0 (B) 100 (C) 140 (D) 200 kV/cm WITH THE E1 AND HH1 ENERGY LEVELS AND CORRESPONDING ENVELOPE WAVEFUNCTIONS.....	13
FIGURE 8	TRANSITION ENERGY SHIFT AS A FUNCTION OF THE ELECTRIC FIELD FOR THE IQW IN FIG. 7 AND CONVENTIONAL QWS OF DIFFERENT THICKNESS.	14
FIGURE 9	SQUARE OF THE OVERLAP INTEGRAL AS A FUNCTION OF THE ELECTRIC FIELD FOR THE IQW AND CONVENTIONAL QWS OF DIFFERENT THICKNESS.....	14
FIGURE 10	SCHEMATIC DIAGRAM OF AN EXEMPLARY DEVICE STRUCTURE OF THE EAM WITH IQWS.....	15
FIGURE 11	NORMALIZED TRANSMISSION OF THE EAM WITH THE CONVENTIONAL QW'S (7.2-nm THICK) AND WITH THE IQW'S. THE DOTS REPRESENT THE HIGHEST SLOPE POINT OF THE CURVE.....	16
FIGURE 12	THE TRANSITION ENERGY SHIFT AS A FUNCTION OF THE APPLIED ELECTRIC FIELD FOR THE 10-nm THICK INGaASP/InGaASP IQW WITH INCREASING INTRA-STEP-BARRIER BANDGAP ENERGY.....	17
FIGURE 13	THE SQUARE OF THE OVERLAP INTEGRAL FOR THE 10-nm THICK INGaASP/InGaASP IQW WITH INCREASING INTRA-STEP-BARRIER BANDGAP ENERGY.....	17
FIGURE 14	ABSORPTION COEFFICIENT OF THE InGa(AL)As/ InAlAs IQW SAMPLE ESTIMATED FROM THE TRANSMISSION MEASUREMENT ON THE RING DIODE.	18
FIGURE 15	MEASURED MODULATOR TRANSFER CURVE (TRANSMISSION MEASURED AT THE REMOTE DETECTOR) AND THE PHOTOCURRENT GENERATED AT THE MODULATOR.....	18

LIST OF TABLES

TABLE 1	BANDWIDTH COMPARISON BETWEEN L-EAM AND TW-EAM.....	5
---------	--	---

Technical Objective:

The main objective of this program was to advance the performance of the semiconductor waveguide modulator in externally modulated RF fiber-optic links for space-based and airborne platforms such as true time delay beam formation and beam steering subsystems in phased array antennas. Device and material approaches were investigated to improve the modulator based on semiconductor structures for achieving high spur free dynamic range (SFDR) and high frequency operation. In these approaches, the semiconductor optical modulators are specifically designed to achieve high slope efficiency and high center frequency, while at the same time maintaining minimal generation of spurious signals. The fiber-optic links using these modulators are expected to satisfy the low noise figure, high center frequencies, low drive power requirements.

This is a collaborative research program in which the University of California at San Diego (UCSD) develops photonic components for fiber links for RF applications. The technical liaison person at Rome Laboratory is Dr. Mike Hayduk. There were two main objectives in this program with respect to the development of the electroabsorption modulator, namely:

1. Attainment of RF transparency of the analog fiber link using the semiconductor electroabsorption waveguide modulator (without amplifier).
2. Enhancing the center frequency of the electroabsorption waveguide modulator to millimeter wave frequencies.

While attaining these objectives, the modulator will maintain the spurious free dynamic range performance as we have previously demonstrated.

The following are the main goals in this year's program:

1. To design and test electroabsorption waveguide modulator for high bandwidth and high slope efficiency and high saturation optical power operation.
2. To collaborate with technical personnel at Air Force Research Laboratory at Rome on the overall link design and provide prototype electroabsorption waveguide modulator for link evaluation.

Summary of Accomplishments

1. We have continued the investigation of the critical design and fabrication issues for broadband traveling wave electroabsorption waveguide modulator. High performance electroabsorption modulator with more than 40 GHz bandwidth has been fabricated and evaluated.
2. We have investigated a new design for quantum well modulator that includes an intra-barrier to enhance the power handling and slope efficiency. Both theory and experiment has been carried out to demonstrate this concept.

Detailed Technical Achievement On Effort

1. Wide Bandwidth Traveling-Wave InGaAsP/InP Electroabsorption Modulator: Measurement and Analysis

High speed and high efficiency electroabsorption modulators (EAMs) are desirable for both analog and digital fiber-optic links. We have previously shown [1] that for maximum RF modulation efficiency, the EAM waveguide is typically limited to 200 ~ 300 μm in length due to the optical propagation loss in the waveguide. This limitation of maximum modulator length also applies to digital link applications where the optical insertion loss of the EAM must be kept low. Our waveguide width is typically designed at ~ 3 μm in order to achieve good optical coupling efficiency with lensed fibers. However, for a lumped-element EAM (L-EAM) with 200 μm long and 3 μm wide waveguide, the modulation bandwidth hardly exceeds 20 GHz even when a 50 ohm shunt resistor is used. To achieve a broader bandwidth, one can either shorten the waveguide length, reduce the waveguide width, increase the waveguide intrinsic layer thickness, or use a smaller shunt resistance. All of these approaches can result in a significant penalty in modulation efficiency. In the past, much effort has been directed to using shorter waveguide for achieving larger bandwidth [2-4]. The shorter-waveguide approach compromises modulation efficiency due to shorter modulation length. For digital links, EAM with very short waveguide may not provide large enough extinction ratio.

The bandwidth for an L-EAM is basically limited by the RC-time constant. To overcome the RC bandwidth limit without severely compromising the modulation efficiency, the traveling wave electroabsorption modulator (TW-EAM) has been proposed and experimentally investigated by several authors [5-7]. However, in these past works, critical issues for the TW-EAM design have not been clarified, and the potential of the traveling-wave effect has not been fully exploited.

The TW-EAM design is distinctly different from the design of other type of traveling-wave modulators (such as LiNbO₃ modulator) due to two reasons: 1). A typical TW-EAM has very low microwave waveguide impedance (~ 20 ohms), slow microwave velocity (phase velocity index ~ 7) and large frequency-dependent microwave attenuation. These factors propose great challenge for the TW-EAM design. Conventional traveling wave design work – including matching the waveguide impedance with 50 ohms, matching the microwave phase velocity with the optical group velocity (index ~ 3.6), and minimizing the frequency dependent microwave loss – is very difficult for TW-EAM. 2). Fortunately, a high-efficiency TW-EAM does not need to be very long, 200 μm length would be enough. This short-length feature greatly eases the above challenging factors for traveling-wave design. It has been predicted that low-impedance-termination for a 200 μm long TW-EAM could achieve ultra broad bandwidth as well as high modulation efficiency [1].

However, many people regard a 200 μm long TW-EAM as basically an L-EAM, thus no advantage can be taken from traveling-wave design for a short device. We clarify this issue both theoretically and experimentally. We derive analytically how a TW-EAM migrates to an L-EAM under the conditions of both short-length and *open-termination*, from which we show that a

properly terminated short-length TW-EAM can break the RC bandwidth limit. We also show our TW-EAM device design based on the above analysis. The measurement results for the fabricated devices include large bandwidth (>40 GHz, limited by the bandwidth of the measurement equipment), high modulation efficiency and high optical saturation power. Microwave properties of the TW-EAM waveguide extracted from the measured data agree very well with the measured frequency response. This confirms our previous theoretical approach in [1].

Theory

In our prior work [1], the TW-EAM modulation frequency response was derived as

$$M(f) = \left| \frac{T}{e^{\gamma_{\mu}L} - \Gamma_L \Gamma_S e^{-\gamma_{\mu}L}} \left\{ \frac{e^{j\beta_o L} - e^{\gamma_{\mu}L}}{(j\beta_o - \gamma_{\mu})L} + \Gamma_L \frac{e^{j\beta_o L} - e^{-\gamma_{\mu}L}}{(j\beta_o + \gamma_{\mu})L} \right\} \times \frac{Z_{JUNCT}}{Z_{SHUNT}} \right|^2 \quad (1)$$

where

Γ_L --- the microwave reflection coefficient in the modulator at the terminator port.

$$\Gamma_L = (Z_L - Z_M) / (Z_L + Z_M).$$

Z_L --- the terminator impedance.

Z_M --- the TW-EAM transmission line impedance.

Γ_S --- the microwave reflection coefficient in the modulator at the source port.

$$\Gamma_S = (Z_S - Z_M) / (Z_S + Z_M).$$

Z_S --- the microwave source impedance.

T --- the transmission coefficient at the source port. $T = 1 - \Gamma_S$.

L --- the modulation length.

γ_{μ} --- the microwave propagation constant. $\gamma_{\mu} = \alpha_{\mu} + j\beta_{\mu}$.

α_{μ} --- the microwave attenuation coefficient.

β_{μ} --- wave number. $\beta_{\mu} = \omega / v_{\mu}$.

ω --- microwave frequency.

v_{μ} --- microwave phase velocity.

$\beta_o = \omega / v_o$, v_o --- optical group velocity.

Z_{JUNCT} --- the junction impedance in the TW-EAM circuit model.

Z_{SHUNT} --- the shunt impedance in the TW-EAM circuit model.

The frequency response in Eq. (1) includes the effects of impedance mismatch, velocity mismatch and microwave loss.

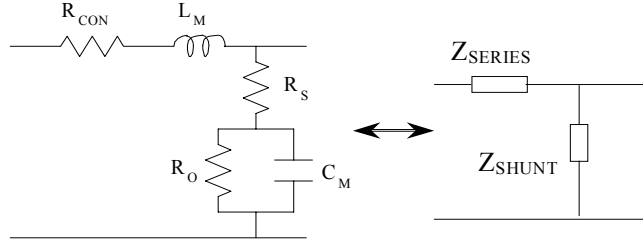


Figure 1 Distributed circuit model for TW-EAM transmission line.

The TW-EAM circuit model plays an important role in our analysis approach. It divides TW-EAM transmission line with any finite length into an *infinite* number of small segments, so that each small segment can be modeled by a lumped-element circuit depicted in Fig. 1. In this circuit model, R_{CON} is the conduction resistance, L_M is the inductance, R_S is the series resistance, C_M is the junction capacitance, and $R_o = (dI_o/dV_j)^{-1}$ is the differential resistance due to the dependence of the photocurrent I_o on the modulator junction voltage V_j . The series impedance Z_{SERIES} (dimension: Ω/mm) and the shunt impedance Z_{SHUNT} (dimension: $\Omega\text{-mm}$) are defined as:

$$Z_{SERIES} = R_{CON} + j\omega L_M, \quad Z_{SHUNT} = R_S + R_o / (1 + j\omega R_o C_M) \quad (2)$$

The junction impedance Z_{JUNCT} includes R_o and C_M . Using this circuit model, the TW-EAM transmission line impedance and its microwave propagation constant can be calculated by:

$$Z_M = \sqrt{Z_{SERIES} Z_{SHUNT}} \quad \gamma_\mu = \alpha_\mu + j\beta_\mu = \sqrt{\frac{Z_{SERIES}}{Z_{SHUNT}}} \quad (3)$$

Now let's examine how the TW-EAM frequency response in Eq. (1) migrates to the L-EAM response when the TW-EAM is short and open-terminated. The open termination makes $\Gamma_L=1$, and the short-length renders the two terms in the bracket of Eq. (1) to ~ 1 . Therefore

$$M(f) \approx \left| \frac{T}{e^{\gamma_\mu L} - \Gamma_S e^{-\gamma_\mu L}} \{1 + 1\} \times \frac{Z_{JUNCT}}{Z_{SHUNT}} \right|^2 \quad (4)$$

Note that $T=1-\Gamma_S$. With small L approximation, we obtain:

$$M(f) \approx \left| \frac{2(1-\Gamma_S)}{(1-\Gamma_S) + \gamma_\mu L(1+\Gamma_S)} \times \frac{Z_{JUNCT}}{Z_{SHUNT}} \right|^2 \quad (5)$$

Applying $(1+\Gamma_S)/(1-\Gamma_S)=Z_S/Z_M$ and $\gamma_\mu/Z_M=1/Z_{SHUNT}$, we can derive

$$M(f) \approx \left| \frac{2Z_{\text{JUNCT}}}{Z_{\text{SHUNT}} + LZ_S} \right|^2 \quad (6)$$

For the sake of simplicity, we assume low optical input power, so that R_o is like an electrical open, and $Z_{\text{JUNCT}} = 1/j\omega C_M$, $Z_{\text{SHUNT}} = R_S + 1/j\omega C_M$. Substituting these terms into Eq. (6), we obtain

$$M(f) \approx \left| \frac{2}{1 + j\omega C_M L(Z_S + R_S/L)} \right|^2 \quad (7)$$

where $C_M L$ is the total capacitance, R_S/L is the total series resistance. The above equation converges to the L-EAM frequency response, with the modulation bandwidth subject to RC limit.

The above derivation shows that a TW-EAM with both short length and open-termination is indeed equivalent to an L-EAM. However, if a short TW-EAM is terminated with *matched-impedance* so that $\Gamma_L \approx 0$, the resulting frequency response will be completely different from Eq. (7). This can be easily understood by re-examining the above derivation. In this case the TW-EAM is not equivalent to an L-EAM, and the bandwidth is no longer subject to RC limit. Therefore, matched-impedance-termination is the most important thing for *short-length* TW-EAM design, velocity matching is not as important because the two terms in the bracket of Eq. (1) are approximately 1 due to the short length.

Table 1 compares the calculated bandwidth for TW-EAM and L-EAM, both using the same waveguide. For a fair comparison, a shunt resistance $R_{\text{sh}} (=Z_L)$ is used for L-EAM. In this case, to calculate the L-EAM modulation bandwidth, the Z_S in Eq. (7) should be replaced by $Z_S R_{\text{sh}} / (Z_S + R_{\text{sh}})$, where $Z_S = 50$ ohms. The table shows that the TW-EAM has great advantage only when it is terminated by a matched impedance (22 ohms). This is consistent with previous analysis.

Table 1 Bandwidth comparison between L-EAM and TW-EAM.

	$Z_L = R_{\text{sh}} = 50 \Omega$	$Z_L = R_{\text{sh}} = 22 \Omega$
L-EAM	20 GHz	30 GHz
TW-EAM	21 GHz	50 GHz

Device Design

Based on the analysis, low-impedance-termination is adopted in our TW-EAM design. An intrinsic bulk- $\text{In}_{1-x}\text{Ga}_x\text{As}_y\text{P}_{1-y}$ absorption layer, with bandgap 1.0 eV ($x=0.24$, $y=0.53$) and thickness $d \sim 0.35 \mu\text{m}$, is sandwiched between two $\sim 1 \mu\text{m}$ thick doped InGaAsP (bandgap 1.08 eV; $x=0.18$, $y=0.40$) layers. The waveguide width is $\sim 3 \mu\text{m}$, waveguide lengths are set at 150 μm , 200 μm and 300 μm , respectively. The waveguide structure forms a large optical cavity to

support a circular-shape fundamental optical mode (plus 3 higher order modes). Simulation shows that when a lensed fiber with 3- μm spot size is aligned to the center of this cavity, 80% of the input power will be coupled into the fundamental mode. The coupled optical power in the fundamental mode remains $>70\%$ when the misalignment is within $\pm 0.5 \mu\text{m}$ in the lateral or vertical direction, and the total power in higher-order modes remains at 10-15%. This good alignment tolerance is due to two reasons: 1) The fundamental mode is larger in size and has a circular shape; 2) the higher-order modes have zero crossing at the center of the optical cavity, with anti-symmetric or near-anti-symmetric mode profile around the center. They also have zero overlap-integral with the fundamental mode (thus the coupling efficiency with fiber mode is small).

After the optical waveguide has been determined, the dimensions related to the electrode should be designed in the view of the microwave properties. In principle, to reduce the microwave loss, the metal width w can be made wider than the waveguide width, with polyimide or other insulating materials applied on the waveguide sidewall for electrical isolation. However, a larger metal width can result in smaller waveguide inductance which will reduce the modulation bandwidth [8]. For our device, w is set slightly less than $3 \mu\text{m}$. The height of the mesa h is $\sim 2 \mu\text{m}$. Although a higher ridge waveguide mesa may provide a larger inductance, it will add series resistance and complicate the fabrication.

Fabrication of the ridge waveguide has been carried out using wet chemical etching with the p-metal as etch mask. Very smooth ridge waveguide sidewall and vertical etching-profile have been achieved, with $\sim 3 \mu\text{m}$ waveguide width after etching undercut. Au/Zn and Au/Ge alloys are used for p- and n-type ohmic contacts, respectively. 500 \AA thick $\text{p}^+\text{-InGaAs}$ layer has been grown on top of the waveguide for smaller contact resistance.

DC Characteristics

Fig. 2 plots the measured transmission and photocurrent against bias voltage for a TW-EAM with $200 \mu\text{m}$ long active length plus a total of $100 \mu\text{m}$ long passive waveguide at the two ends (caused by uncertainty in cleavage position). The input light is 16 mW at $1.32 \mu\text{m}$ wavelength, with TM polarization. The fiber-to-fiber optical insertion loss at zero bias is 11.3 dB . Smaller insertion loss can be obtained by more accurate cleaving and anti-reflection (AR) coating at the facets. The maximum slope efficiency of the normalized transfer curve is 0.65 V^{-1} (equivalent $V_{\pi}=0.5\pi/0.65=2.4\text{V}$) at -0.8 V bias. The above parameters indicate high performance for analog link applications. Further improvement is possible if an MQW absorption layer is used [9]. The polarization dependence of the link RF gain is measured within 2 dB for this device.

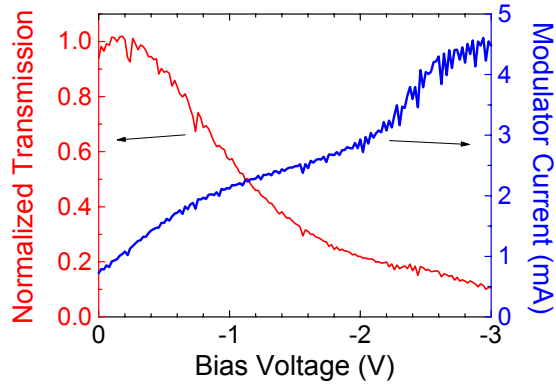


Figure 2 Normalized transmission and modulator current versus bias for a TW-EAM with 200 μm active length plus 100 μm long passive waveguide.

Microwave Properties

The TW-EAM frequency response is determined by the waveguide microwave properties, including waveguide impedance, microwave velocity and microwave loss. To measure these parameters, the TW-EAM is treated as a 2-port microwave device, and the 2-port S-parameters are measured using a 40 GHz network analyzer (HP8510B). Microwave probes at both ports have been calibrated out in a standard full 2-port calibration process.

Microwave properties of the waveguide could possibly be extracted from the measured S-parameters of TW-EAMs with different waveguide lengths. The symmetry of the electrode design results in $S_{12} = S_{21}$ and $S_{11} = S_{22}$ for each TW-EAM, therefore the measured S-parameters for each device only provides 2 independent equations for parameter extraction. During the extraction, a shorter TW-EAM is considered as a cascade of two “pads”, each pad consists of a probing transmission line and one half of the active waveguide length. However, the 2-port S-parameters for each pad (S_{11}^P , S_{22}^P and $S_{21}^P = S_{12}^P$) cannot be solved, since there are 3 unknowns but only 2 independent equations. A longer device, which contains one extra transmission line (active modulation waveguide) between the previously defined two pads, adds 2 more independent equations as well as 2 more unknowns ($S_{11}^0 = S_{22}^0$ and $S_{12}^0 = S_{21}^0$ for the extra active waveguide), so that the problem still remains unsolvable since there are now 5 unknowns but only 4 independent equations.

Combining with a third TW-EAM does not help solve the problem since it does not add any independent equations (its S-parameters can be analytically deduced using the S-parameters of the 1st and the 2nd TW-EAM devices). One might think that we can fabricate a separate “pad”, and then its S-parameters can be measured directly. However, a separate pad is only a 1-port device since there is only one end can be probed, and its 1-port S_{11} simply equals to $S_{11}^1 + S_{21}^1$ (assuming the other end is a perfect open. S_{11}^1 and S_{21}^1 are S-parameters of the shorter TW-EAM), thus it does not add any new information. Therefore, there is no simple way to extract S-parameters for the active waveguide, thus Z_M and γ_μ cannot be completely solved.

Fortunately, there is one simple way to extract γ_μ using transmission matrix approach [10]. The transmission matrix T_1 for the shorter device can be calculated from the measured S-

parameters. On the other hand, it is also a cascade of two “pads” (with unknown transmission matrices P_1 and P_2). The equation between them is:

$$T_1 = P_1 P_2 \quad (8)$$

The transmission matrix T_2 for the longer device can also be calculated from measured data. Similarly, we also have

$$T_2 = P_1 T_0 P_2 \quad (9)$$

where T_0 is the to-be-solved transmission matrix for the extra active waveguide. From Eqs. (8) and (9), we obtain

$$T_2 + T_1 T_2^{-1} T_1 = P_1 (T_0 + T_0^{-1}) P_2 \quad (10)$$

T_0 and T_0^{-1} can be expressed in terms of Z_M and γ_μ [9]:

$$T_0 = \begin{pmatrix} \cosh(\gamma_\mu L_0) & Z_M \sinh(\gamma_\mu L_0) \\ Z_M^{-1} \sinh(\gamma_\mu L_0) & \cosh(\gamma_\mu L_0) \end{pmatrix} \quad (11)$$

$$T_0^{-1} = \begin{pmatrix} \cosh(\gamma_\mu L_0) & -Z_M \sinh(\gamma_\mu L_0) \\ -Z_M^{-1} \sinh(\gamma_\mu L_0) & \cosh(\gamma_\mu L_0) \end{pmatrix} \quad (12)$$

From Eqs. (11) and (12), we find that $T_0 + T_0^{-1}$ becomes a scalar value $2\cosh(\gamma_\mu L_0)$. Thus Eq. (10) becomes

$$T_2 + T_1 T_2^{-1} T_1 = 2\cosh(\gamma_\mu L_0) (P_1 P_2) = 2\cosh(\gamma_\mu L_0) T_1 \quad (13)$$

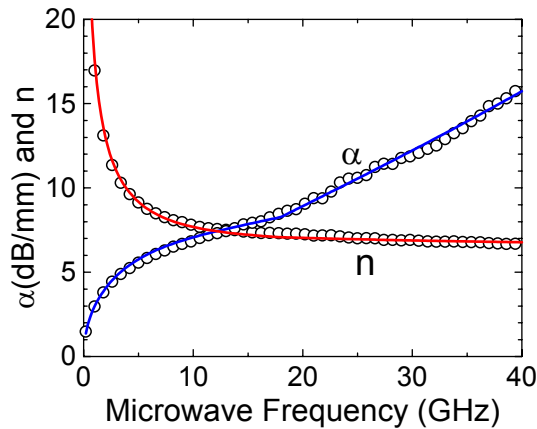


Figure 3 Microwave attenuation factor and phase velocity index of TW-EAM waveguide. Symbols are values extracted from measurement; solid lines are the best-fit using the circuit model shown in Fig. 1.

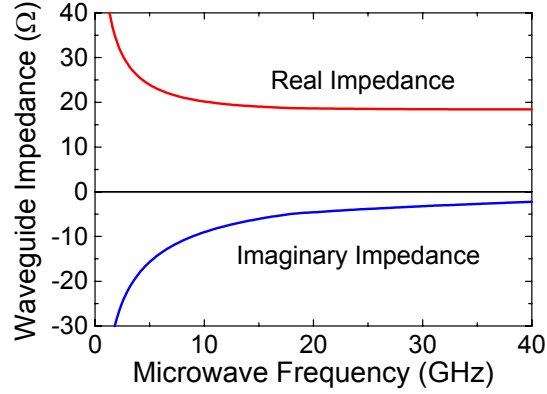


Figure 4 Waveguide impedance of the TW-EAM, calculated using the equivalent circuit model in Fig. 1.

Therefore

$$\cosh(\gamma L_0) = (T_2 T_1^{-1} + T_1 T_2^{-1})/2 \quad (14)$$

The right side of Eq. (14) is a scalar value, although it is calculated from matrices. In this way $\gamma_\mu = \alpha_\mu + j\beta_\mu$ can be solved from T_1 and T_2 . The extracted attenuation factor α_μ and microwave phase velocity index $n_\mu (= \beta_\mu c/\omega)$ are plotted as symbol lines in Fig. 3.

Using the circuit model in Fig. 1 to best-fit the extracted α_μ and n_μ curves in Fig. 3, the following values for the circuit parameters are obtained: $L_M = 0.40$ nH/mm, $R_{CON} = 7.3 \Omega\text{-mm}^{-1}\text{GHz}^{-1/2}$, $R_S = 0.58 \Omega\text{-mm}$, and $C_M = 1.3$ pF/mm. Due to the finite gold thickness ($\sim 0.6 \mu\text{m}$) on top of the waveguide, R_{CON} is assumed to be constant at frequencies below 18 GHz (i.e. $R_{CON} = 7.3 * 18^{1/2} \Omega/\text{mm}$), since $0.6 \mu\text{m}$ is the skin-depth of gold at 18 GHz. Above 18 GHz, R_{CON} is proportional to the square root of frequency. R_o in this case is considered as an open circuit element, as no optical power is used. The calculated α_μ and n_μ curves, plotted as solid lines in Fig. 3, fit the extracted values very well. This supports the proposed distributed circuit model. The active waveguide impedance can also be calculated using the same model and the above circuit parameters. The result is shown in Fig. 4.

After Z_M and γ_μ of the active waveguide are obtained, the microwave properties of the probing transmission lines, which directly impact the modulator frequency response, can be solved from the measured S-parameters of the TW-EAM devices.

Modulation Frequency Response

The 40 GHz network analyzer is used to measure the device frequency response. During the measurement, the probing transmission line at the terminating port of the TW-EAM device is connected to a 50 GHz microwave probe, with 55 ohms shunt resistor (thin-film) soldered on the probe tip. The 2.4-mm connector of this probe is terminated with a 50 ohms broadband load,

giving a total termination impedance of 26 ohms (i.e. 50 ohms in parallel with 55 ohms). The microwave probe at the source port is calibrated out as described in [11].

All the measured frequency response curves show a low-frequency roll-off. This is due to the fact that the waveguide outside the active length has not been passivated, it is a *pin* structure without metal on top of it. The “passive” waveguide contributes to modulation as an active waveguide at very low frequency. However, microwave loss in this “passive” section increases rapidly with frequency, thus its contribution to the modulation rolls off quickly at low frequency. For example, for a device with 150 μm long active section plus 90 μm long total passive section, the effective modulation length is 240 ($=150+90$) μm at DC and it reduces rapidly to 150 μm at slightly higher frequencies. This change of modulation length results in a 4 dB ($=20 \cdot \log(240/150)$) low frequency roll-off. This low frequency roll-off characteristic can be eliminated by waveguide passivation or accurate cleaving.

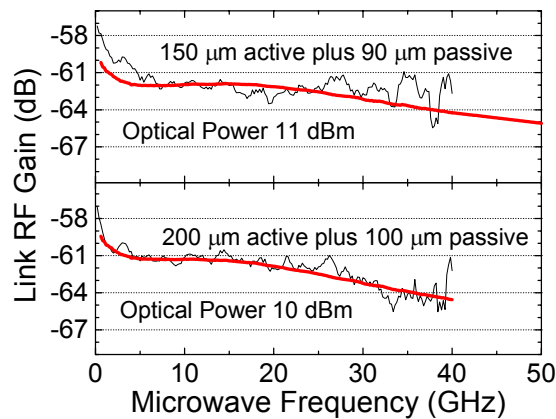


Figure 5 Measured (noisy lines) and calculated (smooth lines) frequency response curves for two TW-EAM devices. The detector responsivity is ~ 0.12 A/W up to 40 GHz

Fig. 5 shows the measured frequency response for the fabricated TW-EAM devices (including the photodetector conversion loss). For the 150 μm long device, the measured 3-dB modulation bandwidth is larger than 40 GHz if the low frequency roll-off is eliminated; For the 200 μm long device, the measured bandwidth is ~ 35 GHz. The frequency response dip at 38 GHz is caused by the detector frequency response. In contrast, for a 200 μm long L-EAM using the same waveguide and 26 Ω shunt resistor, the bandwidth is calculated to be only ~ 25 GHz (including the effect of a contact pad that typically adds 30 fF capacitance. This is consistent because the measured TW-EAM bandwidth also includes the effect of the non-ideal probing transmission lines.) This demonstrates that traveling wave design does provide an advantage for short length EAM device.

To calculate the TW-EAM frequency response, the probing transmission line at the terminating port is considered as part of the termination to the active waveguide while using Eq. (1), and the probing transmission line at the source port is included using cascaded network analysis. The calculated curves, which are also plotted in Fig. 5, fit the measured curves very well, and a 50 GHz modulation bandwidth is predicted for the 150 μm long device. The low-

frequency roll-off in the calculated curves is due to the effect of non-ideal probing transmission lines (because they include the microwave effect of the non-passivated passive section). The non-ideal passive section causes low-frequency roll-off not only by direct contribution to the modulation at low frequency, but also by affecting microwave voltage in the active section, thus it further rolls off the frequency response at low frequency and bend the frequency response at high frequency.

Optical Saturation Power

High optical power operation is desirable for both analog and digital fiber-optic links. The RF gain for analog link using 200 μm long TW-EAM devices (terminated with 26 ohms) is measured against input optical power, with microwave frequency fixed at 18 GHz and detector responsivity of 0.6 A/W. The results are plotted in Fig. 6. The upper curve is for a device biased at -0.8 V with transfer curve slope efficiency of 0.65 V^{-1} ; the lower curve is for another device biased at -1.3 V with slope efficiency of 0.47 V^{-1} . The optical saturation power defined at the 1-dB RF gain compression point is 25 mW for the 1st device and 45 mW for the 2nd device. The difference in the optical saturation power for these two devices is mainly caused by the bias voltage difference. The large optical saturation power for our TW-EAM devices is partially due to the waveguide design, in which the graded band-offset can greatly reduce the hole-piling effect.

At the detector responsivity of 0.6 A/W, the maximum RF gain is about -35 dB for both of the two TW-EAMs, as is shown in Fig. 6. AR coating and accurate cleaving can improve the maximum link RF gain by more than 6 dB.

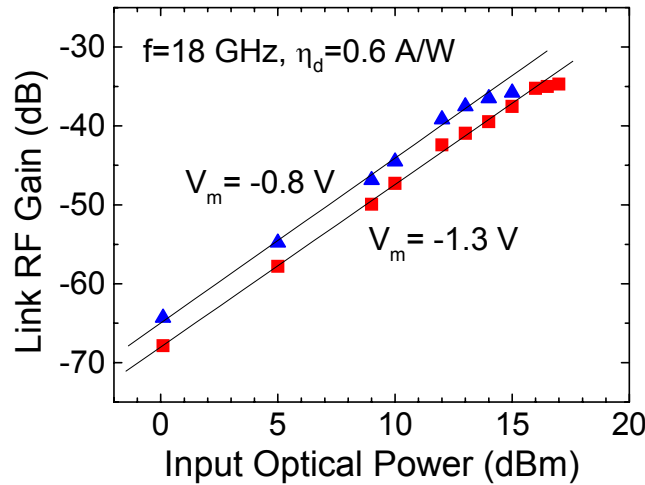


Figure 6 High-frequency optical saturation power for two 200 μm long TW-EAMs with 100 μm long passive length.

2. High-power electroabsorption modulator using intra-step-barrier quantum wells

For an externally modulated analog fiber link, increasing the received optical power reduces the link loss following a quadratic dependence. The optical power used in the link, however, is currently limited by the optical saturation properties of the EAM. Consequently, a concern for the MQW EAM is its relatively low optical saturation power. While the FKE EAM has been shown to saturate beyond 40 mW [12], the conventional MQW EAM, in particular those made of InGaAs/InP, tends to saturate at a much lower level [13].

In quantum wells (QWs), the barriers hinder the sweep-out of the photogenerated carriers, in particular, holes, resulting in carrier pile-up [14]. The traditional approach to reduce this effect had been to use InGaAsP or InAlAs (or InGaAlAs) instead of InP as barrier materials to reduce the valence band offset, which was shown to improve the optical saturation of the MQW EAM [15-18]. Also, there have been attempts to use strain-compensated InGaAsP/InGaAsP and InAsP/GaInP, which have shallow wells, to improve the saturation optical power at 1.55 [19] and 1.3 μm [20]. Although it has been reported that the MQW EAM with InGaAs/InAlAs can handle optical power up to 40 mW without degradation in the bandwidth, the link RF gain was observed to saturate. The maximum optical power that does not cause RF-gain saturation is currently limited to ~ 10 mW [20].

It has also been observed that increasing the electric field reduces the screening effect due to trapped holes. Hence in order to increase the saturation optical power further, the operating bias must be increased for a given intrinsic layer thickness without compromising the slope efficiency. This communication proposes a bandgap-engineering approach that can significantly improve the saturation optical power with enhanced slope efficiency.

Fig. 7 (a) shows the schematic band diagram of the proposed intra-step-barrier quantum well (IQW) for the conduction (E_c) and the valence (E_v) bands with $\text{In}_{0.53}\text{Ga}_{0.47}\text{As}$ well and $\text{In}_{0.52}\text{Al}_{0.48}\text{As}$ barrier, when no electric field is applied. Note that half of the conventional well is replaced by the intra-step-barrier *both* in the conduction and the valence bands, which is formed with a $\text{In}_{0.53}\text{Ga}_{0.33}\text{Al}_{0.14}\text{As}$ ($E_g = 0.97$ eV) layer lattice-matched to InP.

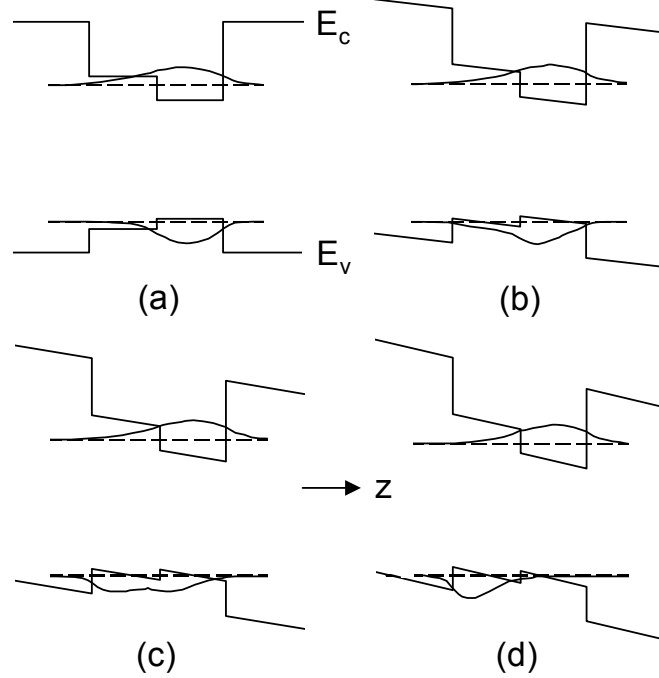


Figure 7 IQWs at different electric field (a) 0 (b) 100 (c) 140 (d) 200 kV/cm with the E1 and HH1 energy levels and corresponding envelope wavefunctions

The IQW structure was analyzed with the finite-difference method using the envelope wavefunctions model under the effective-mass approximation. We only consider the transition from the first heavy-hole state (HH1) to the first electron state (E1).

Fig. 7 (a) to (d) show the IQW structure with energy levels and envelope wavefunctions for a total well width of 10 nm at various electric fields. At zero electric field, the electron in the conduction band is rather loosely confined over the whole well region, while the hole is tightly confined in the deeper intra-well (InGaAs layer), mostly due to the effective mass difference. As the electric field is applied [Fig. 7 (b)] in the $-z$ direction, the electron envelope wavefunction moves in the $+z$ direction, while the hole envelope wavefunction spills over the intra-step-barrier in the $-z$ direction. Up to this point, the overall transition energy shift is very small or even a little positive (blue-shifted). This is because the hole energy level increases with the electric field although the electron energy level decreases. Hence, the normal red-shifted QCSE is effectively suppressed. With the electric field further increased, the energy shift becomes negative (red-shifted), as the hole envelope wavefunction spills further over the intra-step-barrier [Fig. 7 (c)], and the hole energy level starts to decrease. Also the oscillator strength, which is proportional to the square of the spatial overlap integral between the electron and the hole envelope wavefunctions, changes dramatically as the hole envelope wavefunction spills over the intra-step-barrier. At a larger field, [Fig. 7 (d)], the hole is mostly confined over the intra-step-barrier and the oscillator strength becomes very small.

The result is summarized in Fig. 8 for the change in the transition energy and in Fig. 9 for the square of overlap integral as a function of the applied electric field. The results are compared

with the conventional QW with thickness of 7.2 nm and 10.0 nm. The 7.2-nm QW was chosen as a conventional QW for 1.55- μm operation. The 10.0-nm QW was chosen to show the effect of intra-step-barrier, although the zero-field transition energy is not the same as that of the IQW of the same thickness.

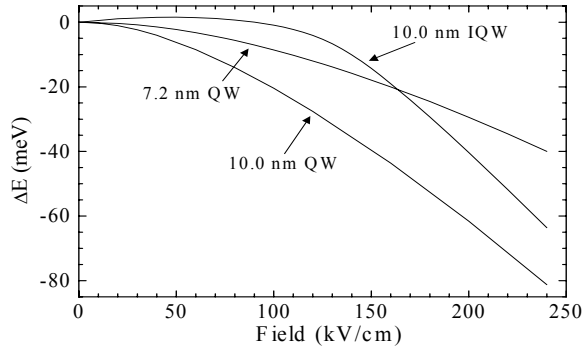


Figure 8 Transition energy shift as a function of the electric field for the IQW in Fig. 7 and conventional QWs of different thickness.

In Fig. 8, it can be seen that the intra-step-barrier effectively suppresses the onset of the red shift of the QCSE up to ~ 100 kV/cm. After ~ 100 kV/cm, the transition energy decreases quickly, crossing that of a 7.2-nm thick conventional QW with a steeper slope. This implies that the EAM with IQWs will be more efficient than that with the conventional QW. When compared with the conventional QW with thickness of 10.0 nm, the slope of the energy shift with respect to the electric field is similar after ~ 100 kV/cm, the curve for the IQW being translated to a higher electric field. Hence the IQW effectively takes advantage of the wider well width, with the delayed onset of the red shift.

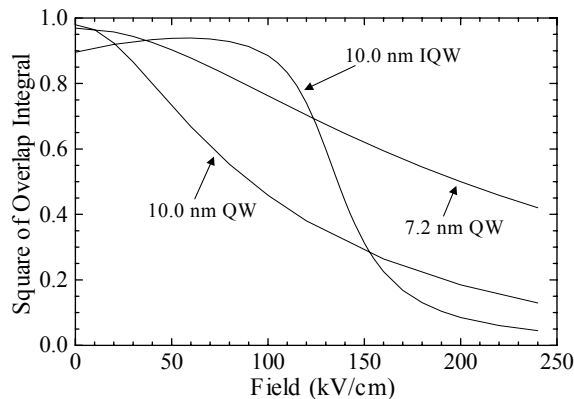


Figure 9 Square of the overlap integral as a function of the electric field for the IQW and conventional QWs of different thickness..

Fig. 9 illustrates a unique feature in the square of the overlap integral of this IQW. This sharp change combined with the energy shift gives a very good QCSE.

With the above results, the change in the absorption coefficient with the electric field was estimated for the 7.2-nm thick conventional quantum well. A simple Gaussian broadening function was used, whose zero-field full width at half maximum (FWHM) was obtained from experimental values (~ 20 meV) [13]. It was varied following the overlap-integral change with the electric field. The absorption coefficient was also estimated from the experimental values. The transfer curve as a function of the applied bias was then calculated for the EAM with intrinsic layer thickness of $0.25 \mu\text{m}$, optical confinement factor of 0.20, and waveguide length of $200 \mu\text{m}$ for $1.55\text{-}\mu\text{m}$ light. The same calculation was repeated for the EAM with the 10.0-nm IQWs with the same device parameters, using the same form of Gaussian broadening. The schematic diagram of the exemplary device structure is shown in Fig. 10. As the zero-field FWHM could not yet be obtained from the experimental values, several values were assumed: 20, 28, and 40 meV. The estimated transfer curves in Fig. 11 show that the EAM with IQWs can be operated at

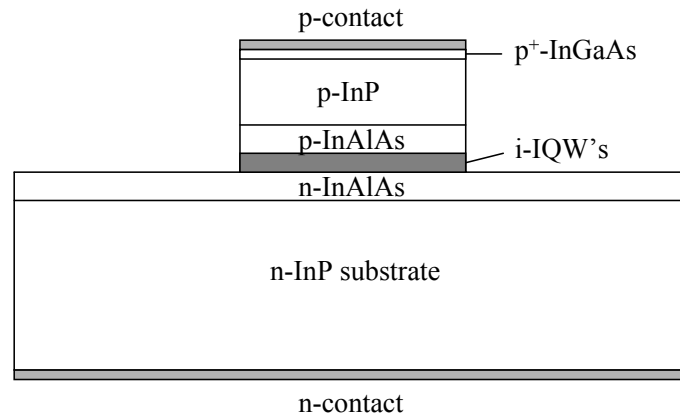


Figure 10 Schematic diagram of an exemplary device structure of the EAM with IQWs.

a higher bias for the highest slope efficiency. For instance, for the FWHM of 20 meV, the highest slope efficiency for the IQW EAM (2.9 V^{-1}) occurs at ~ 2.7 V, while for the conventional QW EAM, it happens at ~ 1.4 V, which represents a factor of ~ 2 increase. Moreover, the slope efficiency itself is increased by a factor of ~ 3.6 with the use of the IQW, which is the consequence of the sharper transition energy shift with the IQW at a higher electric field. This means that the IQW EAM will not only improve the saturation optical power, but also yield a better slope efficiency.

The advantage of using the IQW diminishes as the FWHM value of IQW becomes larger. To get the best results, the interface control should be well maintained, so that the small intra-step-barrier plays the role that had been described in the discussion above.

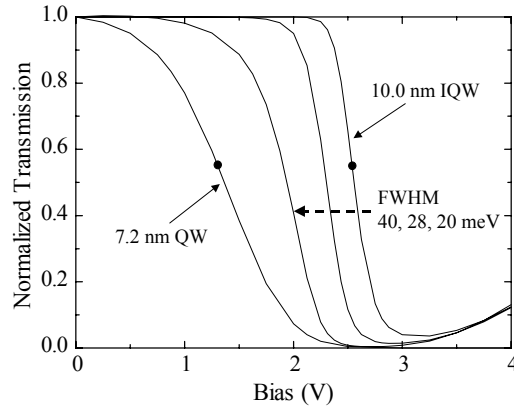


Figure 11 Normalized transmission of the EAM with the conventional QW's (7.2-nm thick) and with the IQW's. The dots represent the highest slope point of the curve.

It is also anticipated that these intra-step-barriers effectively lower the valence band offsets of the InGaAs/InAlAs heterointerface, facilitating the hole escape from the well, further enhancing the high-optical-power operation.

Although the discussion given here is based on the particular material system (InGa(Al)As/InAlAs), it can be applied to other material systems (e.g., InGaAs(P)/InP), with modification on the band offsets, effective masses, and the composition of the well, barrier, and the intra-step-barrier.

Similar calculations (see Figs. 12, 13) have been carried out for the 10-nm thick InGaAsP/InGaAsP IQW lattice-matched to InP. The bandgap energies of the well and the barrier are chosen to be 0.77 and 1.08 eV, and the bandgap energy for the intra-step-barrier is increased from 0.77 (no intra-step-barrier) to 0.82, 0.86, and 0.89 eV. Similar trends as the InGa(Al)As/InAlAs IQW are observed here. At an intra-step-barrier bandgap energy of 0.89 eV, the onset of the red shift is delayed to ~ 100 kV/cm.

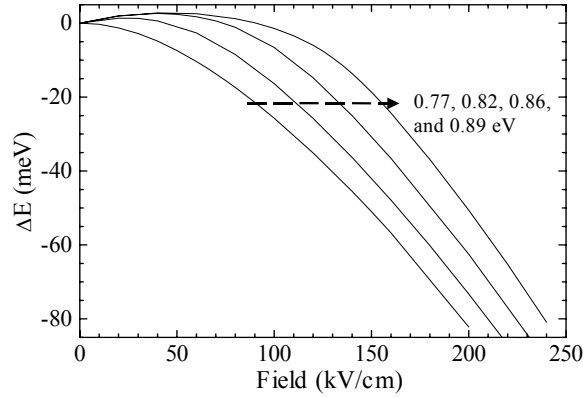


Figure 12 The transition energy shift as a function of the applied electric field for the 10-nm thick InGaAsP/InGaAsP IQW with increasing intra-step-barrier bandgap energy.

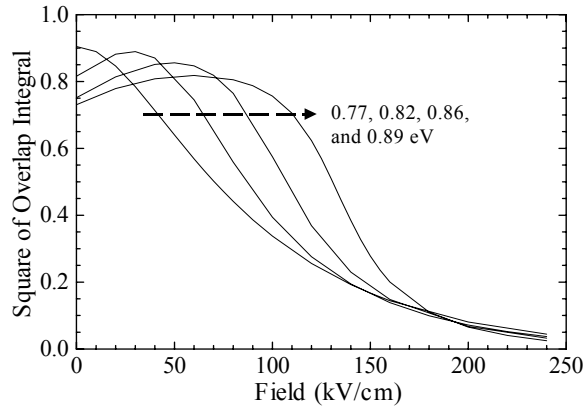


Figure 13 The square of the overlap integral for the 10-nm thick InGaAsP/InGaAsP IQW with increasing intra-step-barrier bandgap energy.

A test IQW EAM structure based on the InGa(Al)As/InAlAs material system was grown by molecular beam epitaxy. The material structure is as follows: a semi-insulating InP substrate, a 0.5- μm n -InAlAs buffer layer ($n = 1 \times 10^{19} \text{ cm}^{-3}$), 13 periods of intrinsic IQW composed of the InAlAs (8 nm)/InGaAs (5 nm)/InGaAlAs (5 nm), an InAlAs (8 nm) barrier, a 1.2- μm p -InAlAs ($p = 2 \times 10^{17} \text{ cm}^{-3}$), and a 50-nm p -InGaAs ($p = 1 \times 10^{18} \text{ cm}^{-3}$) contact layer. The 5-nm thick quaternary InGaAlAs intra-step-barrier was substituted in the growth run by a short superlattice consisting of 5 periods of InGaAs (0.3 nm)/InAlAs (0.7 nm) which has a nominal bandgap energy of $\sim 0.97 \text{ eV}$.

Ring diodes for the surface-normal absorption measurement as well as waveguide EAMs were fabricated from this material. Fig. 14 shows the absorption coefficient (normalized for both the well and barrier) estimated from the transmission measurement of the ring diode. It is observed that in the bias range of 0 to 2 V, the absorption edge due to the exciton remains essentially stationary, signifying the suppression of the red shift as predicted. As the bias is further increased, the absorption edge moves toward the longer wavelengths as in the case of the

conventional QCSE. The absorption in the wavelength range of 1500 – 1600 nm at zero bias is a measurement artifact caused by the absorption in material outside of the IQW layer.

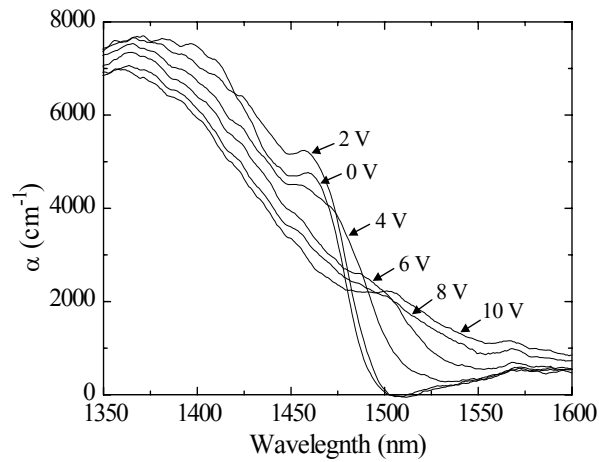


Figure 14 Absorption coefficient of the InGa(Al)As/ InAlAs IQW sample estimated from the transmission measurement on the ring diode.

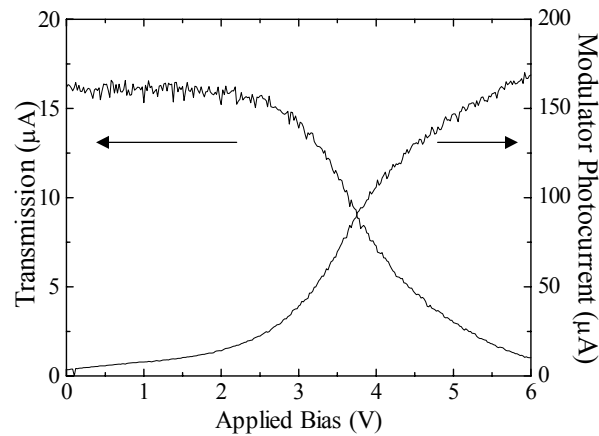


Figure 15 Measured modulator transfer curve (transmission measured at the remote detector) and the photocurrent generated at the modulator.

The transfer curve of the waveguide EAM was measured at the laser wavelength of 1.543 μm and -3 dBm optical power. The waveguide length was 150 μm . Shown in Fig. 15 are the transmission through the EAM detected at the remote detector which has a responsivity of ~ 0.9 A/W and the modulator photocurrent as a function of the applied bias. From the transmission curve, we observe that the onset of the red shift is delayed to ~ 2.5 V. This is consistent with the change of the absorption coefficient as a function of the bias shown in Fig. 14.

References

- [1] G. L. Li, C. K. Sun, S. A. Pappert, W. X. Chen and P. K. L. Yu, "Ultra high-speed traveling wave electroabsorption modulator: design and analysis," *IEEE Trans. MTT, Special issue on "Microwave and Millimeter Wave Photonics"*, vol. 47, pp. 1177-1183, 1999.
- [2] K. Satzke, D. Baums, U. Cebulla, H. Haisch, D. Kaiser, E. Lach, E. Kuhn, J. Weber, R. Weinmann, P. Wiedemann and E. Zielinski, "ultrahigh-bandwidth (42GHz) polarization-independent ridge waveguide electroabsorption modulator based on tensile strained InGaAsP MQW," *Electron. Lett.*, vol. 31, pp. 2030-2032, 1995.
- [3] T. Ido, S. Tanaka, M. Suzuki, M. Koizumi, H. Sano and H. Inoue, "Ultra-high-speed multiple-quantum-well electro-absorption modulators with integrated waveguides," *IEEE J. Lightwave Technol.*, vol. 14, pp. 2026-2034, 1996.
- [4] F. Devaux, S. Chelles, J. C. Harmand, N. Bouadma, F. Huet, M. Carre and M. Foucher, "polarization independent InGaAs/InAlAs strained MQW electroabsorption modulator with 42 GHz bandwidth," *Tech. Dig. 10th Intl. Conf. Integrated Optics and Optical Fiber Comm. (IOOC'95)*, vol. 4, pp. 56-57, 1995.
- [5] H. H. Liao, X. B. Mei, K. K. Loi, C. W. Tu, P. M. Asbeck and W. S. C. Chang, "Microwave structures for traveling-wave MQW electro-absorption modulators for wide band 1.3 μ m photonic links," *Proc. SPIE, Optoelectronic Integrated Circuits*, vol. 3006, pp. 291-300, 1997.
- [6] K. Kawano, M. Kohtoku, M. Ueki, T. Ito, S. Kondoh, Y. Noguchi and Y. Hasumi, "Polarisation-insensitive traveling-wave electrode electroabsorption (TW-EA) modulator with bandwidth over 50 GHz and driving voltage less than 2 V," *Electron. Lett.*, vol. 33, pp. 1580-1581, 1997
- [7] S. Z. Zhang, Y. J. Chiu, P. Abraham and J. E. Bowers, "25-GHz Polarization-insensitive electroabsorption modulators with traveling-wave electrodes," *IEEE Photon. Technol. Lett.*, vol. 11, pp.191-193, 1999.
- [8] G. L. Li, D. S. Shin, W. S. Chang, P. M. Asbeck, P. K. L. Yu, C. K. Sun, S. A. Pappert and R. Nguyen, "Design and fabrication of traveling wave electroabsorption modulator," *Proc SPIE, Optoelectronic Integrated Circuits IV*, vol. 3950, pp. 252-255, 2000.
- [9] D. S. Shin, G. L. Li, C. K. Sun, S. A. Pappert, K. K. Loi, W. S. C. Chang, and P. K. L. Yu, "Optoelectronic RF Signal Mixing Using an Electroabsorption Waveguide as an Integrated Photodetector/Mixer", *IEEE Photonics Technology Letters*, vol. 12, pp. 193-195, 2000.
- [10] D. M. Pozar, "Microwave engineering," Addison-Wesley, pp. 231-235, 1990.
- [11] K.K. Loi, I. Sakamoto, X. F. Shao, H. Q. Hou, H. H. Liao, X. B. Mei, A. N. Cheng, C. W. Tu and W. S. C. Chang, "Accurate de-embedding technique for on-chip small-signal characterization of high-frequency optical modulator," *IEEE Photon. Technol. Lett.*, vol.8, pp.402-404,1996.
- [12] R. B. Welstand, S. A. Pappert, C. K. Sun, J. T. Zhu, Y. Z. Liu, and P. K. L. Yu, *IEEE.Photon. Technol. Lett.* **8**, 1540 (1996).
- [13] S. A. Pappert, R. J. Orazi, T. T. Vu, S. C. Lin, A. R. Clawson, and P. K. L. Yu, *IEEE Photon. Technol. Lett.* **2**, 257 (1990).
- [14] T. H. Wood, J. Z. Pastalan, C. A. Burrus. Jr., B. C. Johnson, B. I. Miller, J. L. deMiguel, U. Koren, and M. G. Young, *Appl. Phys. Lett.* **57**, 1081 (1990).
- [15] F. Devaux, E. Bigan, A. Ougazzaden, F. Huet, M. Carré, and A. Carencu, *IEEE Photon. Technol. Lett.* **4**, 720, (1992).

- [16] A. Ougazzaden, F. Devaux, *Appl. Phys. Lett.* **69**, 4131 (1996).
- [17] T. H. Wood, T. Y. Chang, J. Z. Pastalan, C. A. Burrus, Jr., N. J. Sauer, B. C. Johnson, *Electron. Lett.* **27**, 257 (1991).
- [18] K. Wakita, I. Kotaka, S. Matsumoto, R. Iga, S. Kondo, and Y. Noguchi, *Jpn. J. Appl. Phys.* **37**, 1432 (1998).
- [19] R. Sahara, K. Morito, K. Sato, Y. Kotaki, H. Soda, and N. Okazaki, *IEEE Photon. Technol. Lett.* **7**, 1004 (1995).
- [20] K. K. Loi, I. Sakamoto, X. B. Mei, C. W. Tu, and W. S. C. Chang, *IEEE Photon. Technol. Lett.* **8**, 626 (1996).

Publications

1. G. L. Li, S. A. Pappert, C. K. Sun, W. S. C. Chang, and P. K. L. Yu, "Wide Bandwidth Traveling-Wave InGaAsP/InP Electroabsorption Modulator for Millimeter Wave Applications", Technical Digest of the IMS at Phoenix, May 2001, Paper TU-1C, Vol. 1, p. 61-4, 2001 (Appendix 1).
2. G. L. Li, S. A. Pappert*, P. Mages, C. K. Sun*, W. S. C. Chang, and P. K. L. Yu, "High Saturation, High Speed Traveling-Wave InGaAsP/InP Electroabsorption Modulator", *IEEE Photonic Technology Letters*, Vol. 13, p. 1076-1078, 2001 (Appendix 2)
3. D. S. Shin, W. X. Chen, S. A. Pappert, D. Chow, D. Yap, and P. K. L. Yu, "Analysis of Intra-Step-Barrier Quantum Wells for High-Power Electroabsorption Modulators" International Meeting on Microwave Photonics, MWP'01, Technical Digest, Paper M-2.6, p. 17-20, 2002 (Appendix 3).

Theses supported by this contract:

1. Dongsoo Shin, "High-Efficiency Optical Modulation and Detection for Analog Fiber-Optic Links", UC San Diego, 2001.
2. Guoliang Li, "Wide-Bandwidth High-Efficiency Electroabsorption Modulators for Analog Fiber-Optic Links", UC San Diego, 2002.

Acknowledgments

The work reported here is partially supported by the AFRL program. Additional fundings are obtained from DARPA RFLICS program, the California MICRO program, and ONR.

Wide Bandwidth Traveling-Wave InGaAsP/InP Electroabsorption Modulator for Millimeter Wave Applications

G. L. Li, S. A. Pappert*, C. K. Sun*, W. S. C. Chang, and P. K. L. Yu

University of California, San Diego; Department of ECE; La Jolla, CA 92093-0407

*SPAWAR Systems Center; San Diego, CA 92152-5001

Abstract — Traveling wave electroabsorption modulators (TW-EAMs) can provide large modulation bandwidth and high efficiency features for both analog and digital fiber-optic links. Here, high efficiency TW-EAMs with modulation bandwidths in excess of 40 GHz have been demonstrated. Observing the predicted bandwidth reduction for counter-propagating optical and microwave fields along the waveguide has validated the traveling-wave nature of the modulator.

I. INTRODUCTION

High speed and high efficiency electroabsorption modulators (EAMs) are desirable for both analog and digital fiber-optic links. We have previously reported [1] that for maximum RF modulation efficiency, the EAM waveguide is typically limited to 200 ~ 300 μm in length due to the optical propagation loss in the waveguide. This maximum modulator length limitation also applies to digital link applications where the optical insertion loss of the EAM must be kept low. Our waveguide width is typically designed at ~ 3 μm in order to achieve good optical coupling efficiency with lensed fibers. However, for a lumped-element EAM with 200 μm long and 3 μm wide waveguide, the modulation bandwidth hardly exceeds 20 GHz even when a 50- Ω shunt resistance is used. To achieve a broader bandwidth, one can either shorten the waveguide length, reduce the waveguide width, increase the waveguide intrinsic layer thickness, or use a smaller shunt resistance. All of these approaches result in a significant penalty in modulation efficiency. In the past, much attention has been paid to short EAM waveguides for providing larger bandwidth [2-4]. The short-waveguide approach compromises modulation efficiency due to both shorter modulation length and smaller power handling ability. In digital links, an EAM with very short waveguide may not be able to provide large enough extinction ratio. The bandwidth for a lumped-element EAM is limited by the RC-time constant. To overcome the RC bandwidth limit without severely compromising the modulation efficiency, the traveling wave electroabsorption modulator (TW-EAM) has been proposed and experimentally investigated

by several authors [5-7]. A major challenge of TW-EAM has been the design of a TW structure that will yield high modulation efficiency via large overlap of the modulation field with a thin intrinsic EA layer and a sufficiently high impedance for broadband match to the source with low attenuation at high frequencies. However, to our knowledge, the highest 3-dB electrical bandwidth published for TW-EAM is below 30 GHz [6,7]. This indicates that the potential of the traveling-wave effect has not been fully exploited. In [1], we have proposed several approaches for realizing a high efficiency TW-EAM with bandwidth above 50 GHz. Several important design issues have also been discussed in a later work [8].

In this work, following [1] and [8], we design and fabricate a broadband TW-EAM using the low-impedance termination approach. Excellent DC characteristics are measured for the TW-EAM devices fabricated, indicating high modulation efficiency is achievable. The measured modulation bandwidth for some of the devices is above 40 GHz, limited by the bandwidth of the measurement equipment. Bandwidth reduction is observed when the optical wave and microwave counter-propagate along the waveguide, which is consistent with the traveling-wave effect.

II. DEVICE DESIGN

The optical waveguide geometry for the TW-EAM is designed for maximum modulation efficiency. Fig. 1 shows the waveguide cross-section. The fabrication of the modulator ridge waveguides is done using wet chemical etching. The top metal width (w) is set at 3 μm , and is the same as the waveguide width due to the very smooth sidewall and vertical etching profile of the waveguide mesa.

The intrinsic bulk-InGaAsP (bandgap ~ 1.24 μm) absorption layer thickness is 0.35 μm thick. The absorption layer is sandwiched between two ~ 1 μm thick doped InGaAsP large optical cavity layers for good coupling efficiency with lensed fibers. TW-EAMs with waveguide

lengths of 150 μm , 200 μm and 300 μm , are tested. Fig. 2 shows the top view of the TW-EAM device. 50- Ω CPW microwave connection transmission lines on semi-insulating InP substrate are implemented at the source and the terminator ports to make the electrical connection between the waveguide and microwave probes. Metal connections are made via the polyimide bridges.

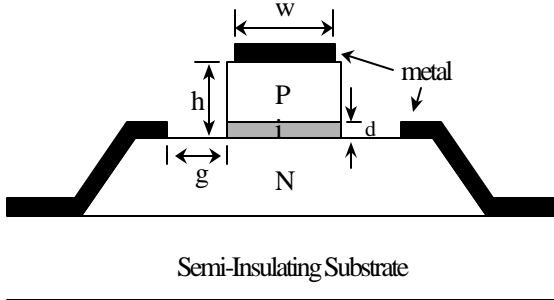


Fig. 1. Cross-section of the TW-EAM waveguide

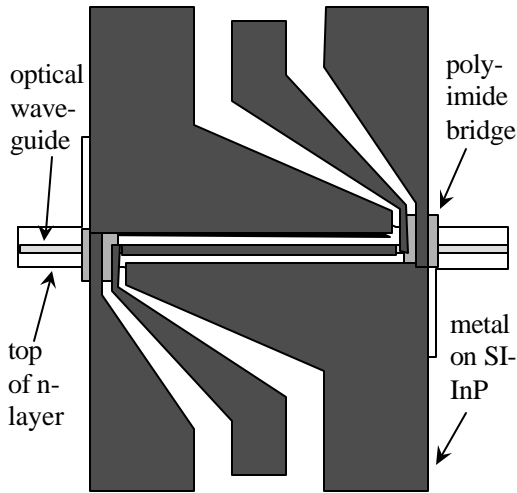


Fig. 2. Top view of the TW-EAM device design.

III. MEASUREMENT RESULTS

A. DC Characteristics

The TW-EAM devices fabricated show good DC characteristics. For a device with 200 μm long modulator length plus 100 μm long passive waveguide (caused by inaccurate cleaving), the fiber-to-fiber optical insertion loss at zero bias is measured to be 11.3 dB with 1.32 μm wavelength light. Smaller insertion loss can be achieved with more accurate cleaving and anti-reflection coating at the facets. The maximum slope efficiency for the transfer

curve normalized at zero bias is measured at 0.65 V^{-1} when the device is biased at -0.8 V . The normalized modulator DC transfer curve remains the same with the optical input power increased up to 20 mW. Since the modulation efficiency is determined by the modulator optical insertion loss, the slope of the transfer curve and the optical saturation power, the above reported DC characteristics result in excellent modulation efficiency for the TW-EAM device.

B. Modulation Frequency Response

A 40 GHz network analyzer HP8510B is used to measure the device frequency response. During the measurement, the terminator port of the TW-EAM devices is contacted by a resistor-shunted 50 GHz CPW microwave probe. The 2.4 mm connector of this probe is terminated by a 50 Ω resistor, giving a total termination impedance of 26.2 Ω for the TW-EAM devices. It is found that the frequency response curves show a low frequency roll-off due to the passive waveguide. This can be explained in light of the absence of metal on top of the passive waveguide, and the p-type layers are relative resistive at frequencies above 5 GHz. For example, for a device with a 150 μm long modulator section and 90 μm long passive waveguide, the effective modulation length is $\sim 240 \mu\text{m}$ for frequencies below $\sim 0.2 \text{ GHz}$ and 150 μm for frequencies above 5 GHz. This modulation length changes give rise to the apparent low frequency roll off ($20 \cdot \log(240/150) = 4.1 \text{ dB}$) The low frequency roll-off characteristic can be eliminated by more accurate cleaving.

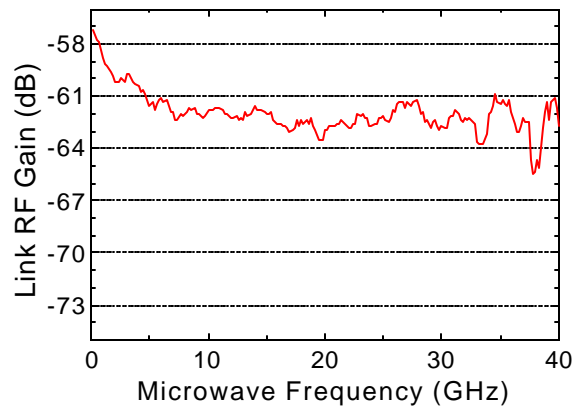


Fig. 3. Frequency response for a 150 μm long TW-EAM with 90 μm long passive waveguide. The input optical power is 11 dBm, detector responsivity is $\sim 0.12 \text{ A/W}$ up to 40 GHz.

The measured frequency response for a 150 μm long TW-EAM device (with 90 μm long passive waveguide) combined with the photodetector loss is shown in Fig. 3. For this measurement, the microwave probe at the source port has been calibrated out. Above 5 GHz, the frequency response does not roll off up to 40 GHz, indicating a modulation bandwidth of above 40 GHz for this TW-EAM device. The frequency response dip at 38 GHz is caused by the detector frequency response. For the 200 μm long device mentioned above, the 3-dB bandwidth is measured at ~ 35 GHz (as shown in top curve of Fig. 4).

It should be noted that the link RF gain in Fig. 3 can be improved 16.5 dB if a photodetector with responsivity of 0.8 A/W is used, instead of one with 0.12 A/W responsivity. Anti-reflection coating on the device facets can improve the link RF gain by another ~ 6 dB, and accurate cleaving can reduce ~ 2 dB RF loss (due to the ~ 1 dB optical loss in the passive waveguide). With these improvements, the link RF gain will be around -37 dB at 40 GHz for the 150 μm long device, with 11 dBm optical power input.

Previously, our group has reported a link RF gain of -17.4 dB for a lumped-element EAM at 1 GHz frequency (AR-coated, with detector responsivity ~ 0.8 A/W and input optical power 43 mW or 16.3 dBm) [9]. The corresponding link RF gain for this lumped-element EAM would be -34 dB if the optical power is scaled down to 11 dBm and a 50- Ω shunt resistor is used (which adds 6 dB RF loss at low frequency).

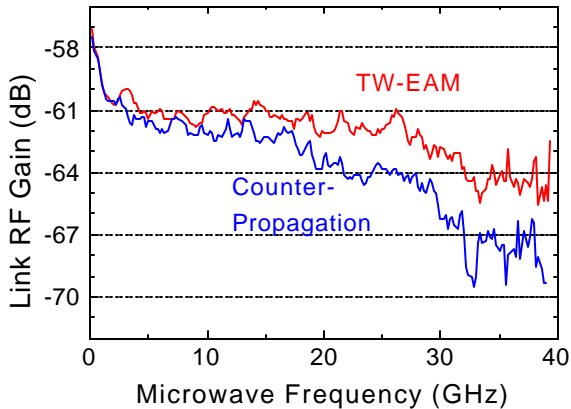


Fig. 4. Frequency response for a 200 μm long TW-EAM with 100 μm long passive waveguide.

C. Counter-Propagation Measurement

In order to confirm the traveling-wave effect in the device, we reverse the optical wave propagation direction

for the 200 μm long device so that the optical wave and microwave counter-propagate along the waveguide. In this case the 3-dB bandwidth is measured at ~ 25 GHz, which is 10 GHz smaller than the ~ 35 GHz bandwidth of the normal TW-EAM device. The measured frequency responses are shown in Fig. 4. The bandwidth reduction in the counter-propagation measurement is consistent with the traveling-wave effect predicted for TW-EAM.

D. Return Loss

The return loss (S_{11}) of an EAM is often an important concern in a practical system. The desirable S_{11} is as small as possible, so that the microwave source will not be affected by the reflected microwave power. By using a 50- Ω shunt resistor for lumped-element EAMs, very small S_{11} can be achieved at low frequency. However, at high frequency, the impedance of the EAM is very small (~ 5 Ω for a 200 μm long and 3 μm wide waveguide), so that the 50- Ω shunt resistor does not help much to reduce S_{11} . This is illustrated in Fig. 5. The measured S_{11} for the TW-EAM device terminated with 26.2 Ω is also shown in the same figure. An interesting observation is that a smaller S_{11} is obtained for the TW-EAM device at frequencies above 5 GHz. This can be explained by the fact that the input impedance of the terminated TW-EAM device has different frequency dependence than that of the lumped-element EAM [1].

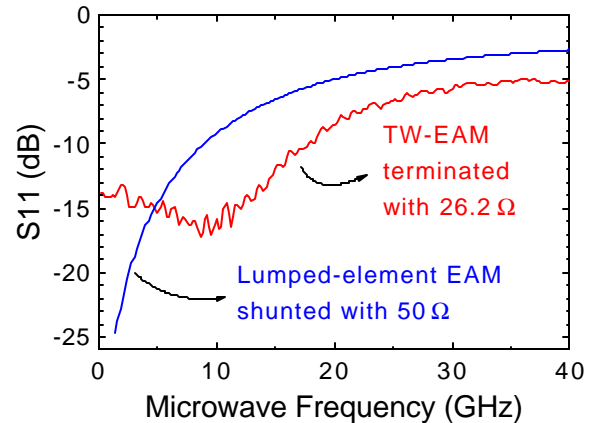


Fig. 5. Measured S_{11} of the TW-EAM compared with calculated S_{11} for lumped-element EAM shunted with 50- Ω .

E. Microwave Properties of the Waveguide

In terms of microwave properties, the TW-EAM waveguide shown in Fig. 1 is different from either a coplanar waveguide or a micro-strip waveguide. The microwave velocity is much slower in the TW-EAM

waveguide due to larger capacitance [1,5]. The TW-EAM modulation frequency response is determined by the waveguide microwave properties, including waveguide impedance, microwave velocity and microwave loss [1]. To measure these microwave parameters, the TW-EAM device can be treated as a two-port microwave device due to the electrode design shown in Fig. 2. The two-port S-parameters can be measured for TW-EAM devices with different waveguide length, so that the effect of the contact pads can be calibrated out and the microwave properties for the waveguide can be extracted. The extracted microwave parameters for the waveguide can be fed into the theoretical formula in [1] to calculate the modulation frequency response. In this way, the theory can be compared with the measurement results. Fig. 6 shows the typical microwave loss (or S_{21}) measured for TW-EAM devices with different waveguide length. From this figure we can see that the microwave loss due to the waveguide is pretty small. The parameter-extraction for the microwave properties of the waveguide will be presented at the conference.

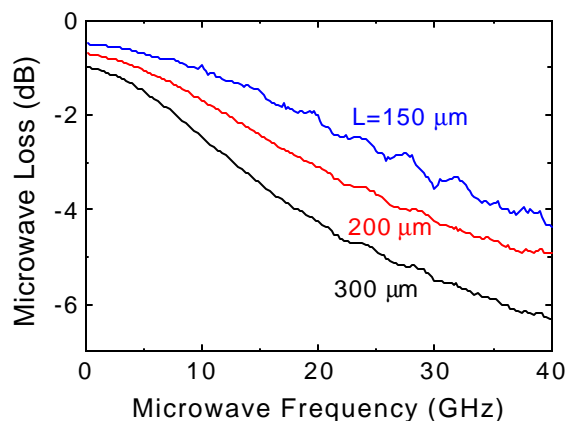


Fig. 6 Measured microwave loss for TW-EAM devices with different waveguide length.

IV. CONCLUSION

Wide bandwidth and high efficiency TW-EAM devices have been designed and fabricated according to our previously proposed low-impedance-termination approach. For the 150 μm long device, an electrical modulation bandwidth is measured above 40 GHz, limited by the measurement equipment. As expected, bandwidth reduction is observed when the optical wave and microwave counter-propagate along the waveguide. The modulation efficiency at 40 GHz for our TW-EAM is comparable to the modulation efficiency at low frequency

for the reported lumped-element EAM using the same measurement setting. Improvement in modulation efficiency can be obtained by employing multiple quantum wells in the modulation layer. The results indicate that the traveling-wave EAM design is a very promising and practical approach for broadband millimeter wave as well as high-speed communication applications.

ACKNOWLEDGEMENT: This work is supported by AFRL, ONR and MICRO/Raytheon Program of California. The authors also wish to thank the following colleagues at UCSD and SPAWAR for their assistance: D. S. Shin, F. Lu, Y. M. Kang, P. Mages, R. Nguyen and Y. Wu.

REFERENCES

- [1] G. L. Li, C. K. Sun, S. A. Pappert, W. X. Chen and P. K. L. Yu, "Ultra high-speed traveling wave electroabsorption modulator: design and analysis," *IEEE Trans. MTT, Special issue on "Microwave and Millimeter Wave Photonics"*, vol. 47, pp. 1177-1183, 1999.
- [2] K. K. Loi, X. B. Mei, J. H. Hodiak, C. W. Tu and W. S. C. Chang, "38 GHz bandwidth 1.3 μm MQW electroabsorption modulators for RF photonic links," *Electron. Lett.*, vol. 34, pp. 1018-1019, 1998.
- [3] T. Ido, S. Tanaka, M. Suzuki, M. Koizumi, H. Sano and H. Inoue, "Ultra-high-speed multiple-quantum-well electro-absorption modulators with integrated waveguides," *IEEE J. Lightwave Technol.*, vol. 14, pp. 2026-2034, 1996.
- [4] A. Stöhr, R. Heinzlmann, R. Buß and D. Jäger, "Electroabsorption Modulators for Broadband Fiber Electro-Optic Field Sensors," *Applications of Photonic Technology 2, Plenum Press*, pp. 871-876, 1997.
- [5] H. H. Liao, X. B. Mei, K. K. Loi, C. W. Tu, P. M. Asbeck and W. S. C. Chang, "Microwave structures for traveling-wave MQW electro-absorption modulators for wide band 1.3 μm photonic links," *Proc. SPIE, Optoelectronic Integrated Circuits*, vol. 3006, pp. 291-300, 1997.
- [6] K. Kawano, M. Kohtoku, M. Ueki, T. Ito, S. Kondoh, Y. Noguchi and Y. Hasumi, "Polarisation-insensitive traveling-wave electrode electroabsorption (TW-EA) modulator with bandwidth over 50 GHz and driving voltage less than 2 V," *Electron. Lett.*, vol. 33, pp. 1580-1581, 1997.
- [7] S. Z. Zhang, Y. J. Chiu, P. Abraham and J. E. Bowers, "25-GHz Polarization-insensitive electroabsorption modulators with traveling-wave electrodes," *IEEE Photon. Technol. Lett.*, vol. 11, pp.191-193, 1999.
- [8] G. L. Li, D. S. Shin, W. S. Chang, P. M. Asbeck, P. K. L. Yu, C. K. Sun, S. A. Pappert and R. Nguyen, "Design and fabrication of traveling wave electroabsorption modulator," *Proc SPIE*, vol. 3950, pp. 252-255, 2000.
- [9] R. B. Welstand, S. A. Pappert, C. K. Sun, J. T. Zhu, Y. Z. Liu and P. K. L. Yu, "Dual-function electroabsorption waveguide modulator/detector for optoelectronic transceiver applications," *IEEE Photon. Technol. Lett.*, vol.8, pp.1540-1542,1996.

High Saturation, High Speed Traveling-Wave InGaAsP/InP Electroabsorption Modulator

G. L. Li, S. A. Pappert*, P. Mages, C. K. Sun*, W. S. C. Chang, and P. K. L. Yu

University of California, San Diego; Department of ECE; La Jolla, CA 92093-0407

*SPAWAR Systems Center; San Diego, CA 92152-5001

Abstract- High saturation power, traveling-wave electroabsorption modulators (TW-EAMs) with modulation bandwidth greater than 40 GHz have been demonstrated. Microwave properties of the TW-EAM waveguide are extracted from the measured S-parameters using the equivalent circuit model in ref. 4. Excellent agreement is obtained between the predicted and the measured frequency responses.

Index Terms: Electroabsorption, traveling-wave modulator, broad band modulation, high saturation.

Traveling-wave electroabsorption modulators (TW-EAMs) can provide high-speed and high-efficiency features desirable for analog and digital fiber-optic links [1-5]. The major design concerns for the TW-EAM have been its low microwave waveguide impedance, slow microwave velocity and large frequency-dependent microwave attenuation. In a previous work [4], we have established a comprehensive theoretical approach for analyzing the TW-EAM frequency response, including effects of impedance mismatch, velocity mismatch and microwave attenuation. In [4], a distributed equivalent RF circuit model had been developed for representing the TW-EAM waveguide, with several practical approaches proposed for realizing a high efficiency TW-EAM with wide bandwidth.

In this work we demonstrate a broadband TW-EAM using the low-impedance-termination approach. High slope efficiency and high optical saturation power have been achieved for fabricated devices. Also, excellent agreement is obtained between the measured frequency response and that predicted from traveling wave analysis. The modulation bandwidth is more than 40 GHz, and is limited by the bandwidth of equipment.

The TW-EAM employs the Franz-Keldysh effect in InGaAsP, with the PIN layers grown on semi-insulating InP. In our design of the TW-EAM optical waveguide, particular attention is paid to the modulation efficiency. The material structure, in terms of layer thickness and composition, is optimized with respect to both the modulator slope efficiency and the coupling between the optical waveguide and the fiber [5]. The intrinsic InGaAsP layer, with background doping below 10^{16} cm^{-3} , has a

bandgap of 1 eV and a thickness of $0.35 \mu\text{m}$, and is sandwiched between two $\sim 1 \mu\text{m}$ thick doped InGaAsP (1.08 eV bandgap) layers to form a large optical cavity. The doping concentration is around $2 \times 10^{18} \text{ cm}^{-3}$ for n-type layers, and graded from 5×10^{17} to $2 \times 10^{18} \text{ cm}^{-3}$ for p-type layers. To further facilitate the coupling to tapered fibers with $3\text{-}\mu\text{m}$ (diameter) spot size, the optical waveguide width is chosen to be $3 \mu\text{m}$. The length of the electrode ranges from 150 to $300 \mu\text{m}$. Vertical, smooth sidewalls of the mesa have been achieved through wet chemical etching. Fig. 1 shows the schematic top view of the TW-EAM. The $50\text{-}\Omega$ CPW microwave connection transmission lines on semi-insulating InP are made at the source and the termination ports to connect to microwave probes. Ground electrodes are connected via the n-layer and metal connections on top of the polyimide (see Fig. 1). The center electrodes of the CPWs are connected to the p-electrode of the modulator via polyimide bridges.

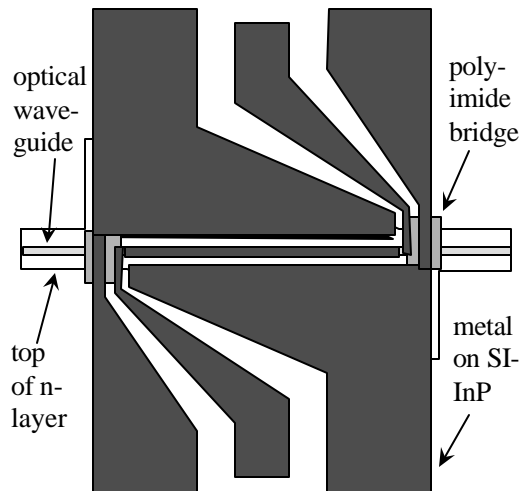


Fig. 1. Schematic top view of the TW-EAM showing the microwave electrodes and the optical waveguide.

The TW-EAMs show good DC characteristics. For a device with $200 \mu\text{m}$ long electrode length plus $100 \mu\text{m}$ long passive waveguide (caused by uncertainties in cleavage positions), the fiber-to-fiber optical insertion loss at zero

bias has been measured to be 11.3 dB (at 1.32 μm wavelength). From the normalized transfer curve of this device, a slope efficiency of 0.65 V^{-1} has been obtained at -0.8 V bias. The slope efficiency can be enhanced if MQW absorption layer is used.

For the electrode structure shown in Fig. 1, the device can be considered as a two-port microwave device. A 40 GHz network analyzer (HP8510B) has been used to measure the two-port S-parameters for TW-EAMs with different electrode lengths. The microwave probes at both ports has been first calibrated out in a standard full two-port calibration process. The microwave propagation constant $\gamma(=\alpha+j\beta)$ for the waveguide is then extracted using the ABCD transmission matrix approach [6]. The resulting microwave attenuation factor α and microwave phase velocity index $n(=\beta c/\omega)$ are plotted in Fig. 2.

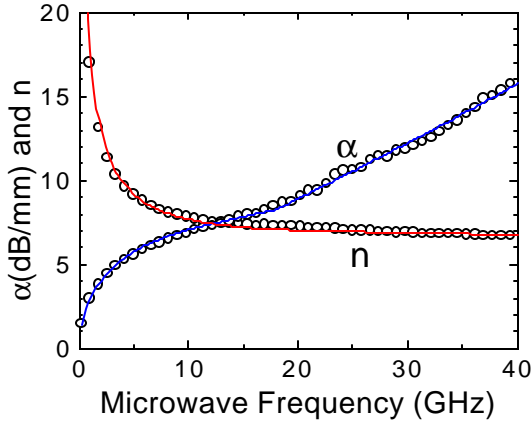


Fig. 2. Microwave attenuation factor and phase velocity index of TW-EAM waveguide. Symbols represent values extracted from measured S-parameters; solid lines are best-fittings using the equivalent circuit model in [4].

Using the quasi-static equivalent circuit model in [4], the following circuit parameters for a unit length of TW-EAM microwave transmission line are derived by best-fitting the α and n values, as shown by the solid lines in Fig. 2: the inductance $I_m = 0.40 \text{ nH/mm}$; the conduction resistance $R_{\text{con}} = 7.3 \text{ } \Omega\text{-mm}^{-1}\text{GHz}^{-1/2}$; the device series resistance $R_s = 0.58 \text{ } \Omega\text{-mm}$; and the junction capacitance $C_m = 1.3 \text{ pF/mm}$. Due to the finite gold thickness ($\sim 0.6 \text{ } \mu\text{m}$) on top of the waveguide, R_{con} is assumed to be a constant at frequencies below 18 GHz (i.e. $R_{\text{con}} = 7.3 \cdot 18^{1/2} \text{ } \Omega/\text{mm}$). Above 18 GHz, R_{con} is proportional to the square root of frequency. To represent the dependence of the modulator current on the junction voltage, a R_0 in parallel with C_m is used to designate the equivalent ac resistance due to the

averaged optical absorption. Fig. 3 depicts the calculated TW-EAM microwave waveguide impedance at zero optical input using the above circuit parameters.

After the microwave properties of the PIN waveguide have been obtained, the microwave parameters of the connection CPW transmission lines on top of the semi-insulating InP substrate can be deduced. These transmission lines at both source and termination ports are included in calculating the TW-EAM modulation frequency response using the analysis in [4]. In the same equivalent circuit model, R_0 at a given optical input level can be estimated from the slope of the EAM DC photocurrent versus voltage curves ($R_0 \sim 300 \text{ } \Omega\text{-mm}$ at 10 dBm input optical power).

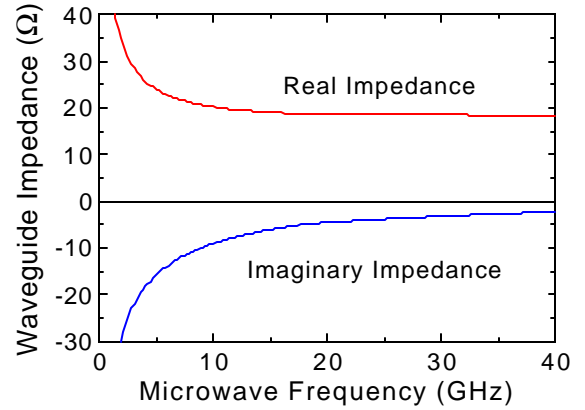


Fig. 3. Waveguide impedance calculated from equivalent circuit model for the fabricated TW-EAM.

For the frequency response measurement, the termination port of the TW-EAM devices is contacted by a 50 GHz microwave probe that provides a termination impedance of $26.2 \text{ } \Omega$. It is found that the frequency response curves show a low frequency roll-off due to the passive optical waveguide. This is mainly due to the absence of metal on top of the passive waveguide, so that the microwave loss in the passive waveguide increases much faster with frequency. For example, for a device with $150 \text{ } \mu\text{m}$ long electrode length and $90 \text{ } \mu\text{m}$ long passive waveguide, the effective modulation length is $\sim 240 \text{ } \mu\text{m}$ for frequencies below $\sim 0.2 \text{ GHz}$ and $150 \text{ } \mu\text{m}$ for frequencies above 5 GHz . This modulation length change gives rise to the apparent low frequency roll-off ($20 \cdot \log(240/150) = 4.1 \text{ dB}$). The low frequency roll-off characteristic can be eliminated by more accurate cleaving.

The measured frequency response for TW-EAM devices (with the passive waveguide) including the photodetector conversion loss is shown in Fig. 4. The

microwave probe at the source port has been calibrated out. For the 150 μm long device, the 3-dB modulation bandwidth is larger than 40 GHz. For the 200 μm long device, the bandwidth is measured at ~ 35 GHz. The calculated TW-EAM frequency responses are also plotted in Fig. 4. The calculated curves fit the measured curves very well, and a 50 GHz modulation bandwidth is predicted for the 150 μm long device.

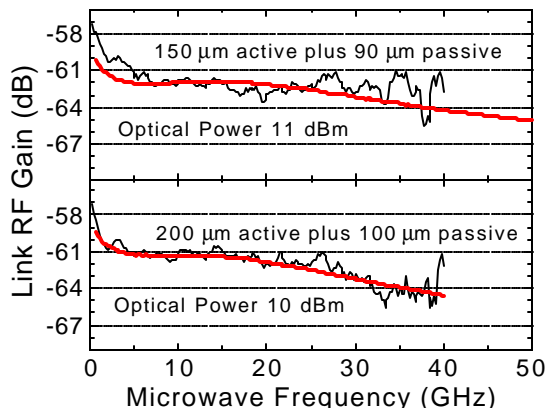


Fig. 4. Measured (thin noisy lines) and calculated (thick smooth lines) frequency responses for two TW-EAM devices. The detector responsivity is ~ 0.12 A/W up to 40 GHz.

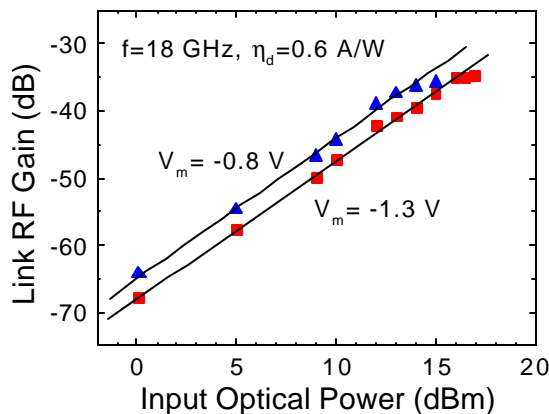


Fig. 5. High frequency optical saturation power for two 200 μm long TW-EAMs with 100 μm long passive waveguide.

Link RF gain using 200 μm long TW-EAM devices (terminated with 26.2 Ω) is measured against input optical power, with microwave frequency fixed at 18 GHz and detector responsivity of 0.6 A/W. The results are plotted in Fig. 5. The top curve is for a device biased at -0.8 V with

transfer curve slope efficiency of 0.65 V $^{-1}$; while the bottom curve is for another device biased at -1.3 V with the slope efficiency of 0.47 V $^{-1}$. The optical saturation power at 1-dB RF gain compression point is 25 mW for the 1st device and 45 mW for the 2nd device. The difference of the saturation power for these two devices is mainly caused by the 0.5 V bias difference. Comparing with lumped element EAM having the same bandwidth, TW-EAM has longer waveguide length, so that its optical absorption is more distributed. This leads to the higher saturation power of TW-EAM. The high saturation power of our TW-EAM devices is also contributed by the design of layer structure with graded band-offset due to epitaxy, so that the hole-piling effect is reduced. At the photodetector responsivity of 0.6 A/W, the maximum RF gain is about -35 dB for both of the above TW-EAM devices. AR coating and more accurate cleaving can improve the RF link gain.

In summary, wide bandwidth and high efficiency InGaAsP/InP TW-EAM devices have been designed and fabricated according to our previously proposed low-impedance-termination approach. Improvement in modulation efficiency can be obtained by using multiple quantum well material in the modulation layer. The results indicate that the traveling-wave EAM design is a very promising and practical approach for broadband millimeter wave as well as high-speed communication applications.

ACKNOWLEDGEMENT: This work is supported by AFRL, ONR and Raytheon/MICRO Program of California.

REFERENCES

- [1] H. H. Liao, X. B. Mei, K. K. Loi, C. W. Tu, P. M. Asbeck and W. S. C. Chang, "Microwave structures for traveling-wave MQW electro-absorption modulators for wide band 1.3 μm photonic links," *Proc. SPIE, Optoelectronic Integrated Circuits*, vol. 3006, pp. 291-300, 1997.
- [2] K. Kawano, M. Kohtoku, M. Ueki, T. Ito, S. Kondoh, Y. Noguchi and Y. Hasumi, "Polarisation-insensitive traveling-wave electrode electroabsorption (TW-EA) modulator with bandwidth over 50 GHz and driving voltage less than 2 V," *Electron. Lett.*, vol. 33, pp. 1580-1581, 1997.
- [3] S. Z. Zhang, Y. J. Chiu, P. Abraham and J. E. Bowers, "25-GHz Polarization-insensitive electroabsorption modulators with traveling-wave electrodes," *IEEE Photon. Technol. Lett.*, vol. 11, pp. 191-193, 1999.
- [4] G. L. Li, C. K. Sun, S. A. Pappert, W. X. Chen and P. K. L. Yu, "Ultra high-speed traveling wave electroabsorption modulator: design and analysis," *IEEE Trans. MTT.*, vol. 47, pp. 1177-1183, 1999.
- [5] G. L. Li, D. S. Shin, W. S. Chang, P. M. Asbeck, P. K. L. Yu, C. K. Sun, S. A. Pappert and R. Nguyen, "Design and fabrication of traveling wave electroabsorption modulator," *Proc SPIE, Optoelectronic Integrated Circuits IV*, vol. 3950, pp. 252-255, 2000.
- [6] D. M. Pozar, "Microwave engineering," Addison-Wesley, pp. 231-235, 1990.

Analysis of Intra-Step-Barrier Quantum Wells for High-Power Electroabsorption Modulators

D. S. Shin, W. X. Chen, S. A. Pappert*, D. Chow**, D. Yap**, and P. K. L. Yu
University of California, San Diego; Department of ECE; La Jolla, CA 92093-0407

* SPAWAR Systems Ctr.; San Diego, CA 92152-5001

**HRL; Malibu, CA 90265

Abstract: We present analysis and preliminary experimental results of intra-step-barrier quantum wells for high-saturation-optical-power electroabsorption modulators. We have shown that the intra-step-barrier delays the onset of red shift in the quantum-confined Stark effect to a higher field.

Summary

The electroabsorption modulator (EAM) with high saturation optical power is currently receiving considerable attention, as microwave fiber-optic link performance is known to improve with increasing optical power incident on the modulator. In particular, the RF link gain in an analog fiber-optic link increases quadratically with the optical power.

The EAM with a multiple-quantum-well (MQW) active layer, which is very popular due to its large absorption-coefficient change with applied electric field, has shown relatively low saturation optical power [1]. It has been pointed out that the field-screening effect due to the trapped photogenerated carriers in the well causes the saturation in the EAM [2]. Although EAMs with improved saturation properties have been demonstrated through lower barrier heights or strains applied at the well and the barrier [3-8], the highest incident optical power level on the MQW EAM that does not result in RF-gain compression is still limited to ~10 mW [8].

Recently, we have proposed the use of a step barrier inside the well to suppress the onset of the red shift in the quantum-confined Stark effect (QCSE) to a higher electric field to enhance the

saturation optical power of the EAM [9]. By delaying the red shift with the proposed intra-step-barrier quantum wells (IQWs), the biasing electric field for the EAM can be increased without compromising the modulation efficiency. As the screening effect due to the photogenerated carriers is reduced at higher electric field, the EAM with the IQWs can be operated at higher optical power, which can improve the fiber-link performance substantially.

In this paper, we describe the effect of the step barrier height on the electroabsorption characteristics in both InGa(Al)As/InAlAs and InGaAsP/InGaAsP quantum wells (QWs). The transition energy and the square of the overlap integral for both types of QWs are investigated.

The IQW structure was analyzed with the finite-difference method. The envelope wavefunction model under the effective-mass approximation was employed for both the conduction and valence bands. The effect of the intra-step-barrier is most noticeable for the transition from the first heavy-hole state (HH1) to the first electron state (E1).

We also obtained preliminary experimental results on the EAM with InGa(Al)As/InAlAs IQWs, including the modulator transfer curve, which confirms the effect of the intra-step-barrier.

Figure 1 (a) - (d) show the schematic band diagrams of the 10-nm thick IQW with an In_{0.53}Ga_{0.47}As ($E_g = 0.75$ eV) well, In_{0.52}Al_{0.48}As barriers ($E_g = 1.47$ eV), and an In_{0.53}Ga_{0.33}Al_{0.14}As ($E_g = 0.97$ eV) intra-step-barrier lattice-matched to InP, with and without the electric field. Also shown are the energy levels

and the envelope wave functions associated with E1 and HH1.

At zero electric field, it is seen that the heavy hole is more tightly confined in the well than the electron is. This is mainly due to the large effective-mass difference between the electron and the heavy hole. As the electric field is increased, the electron energy level decreases in a usual manner of the Stark shift. On the other hand, the hole energy level increases initially to overcome the intra-step-barrier. This effectively suppresses the red shift in the transition energy. As the hole becomes more confined in the region of the intra-step-barrier, the hole energy level starts to decrease and the overall transition energy then undergoes red shift.

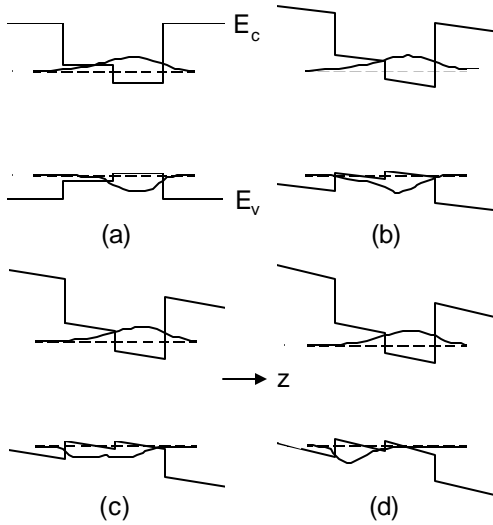


Fig. 1. InGa(Al)As/InAlAs IQW at different electric field (a) 0, (b) 100, (c) 140, and (d) 200 kV/cm with the E1 and HH1 energy levels and the corresponding envelope wave functions.

Figures 2 and 3 show results on the 10-nm thick InGa(Al)As/InAlAs IQW. The transition energy shift (Fig. 2) and the square of the overlap integral between the electron and the heavy-hole envelope wave functions (Fig. 3) are shown as a function of the electric field. The intra-step-barrier bandgap energy is increased from 0.75 (no intra-step-barrier) to 0.82, 0.89, and 0.97 eV. It is seen that the onset of the red shift and the sharp change in the square of the overlap integral are delayed to a higher electric field with the

increasing intra-step-barrier bandgap energy. At an intra-step-barrier bandgap energy of 0.97 eV, the onset of the red shift is delayed to ~ 100 kV/cm.

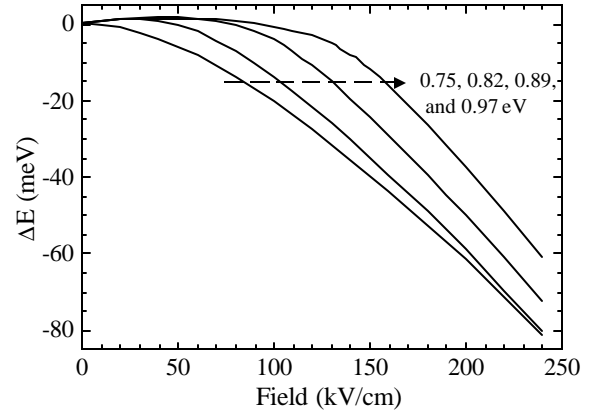


Fig. 2. The transition energy shift as a function of the applied electric field for the 10-nm thick InGa(Al)As/InAlAs IQW with increasing intra-step-barrier bandgap energy.

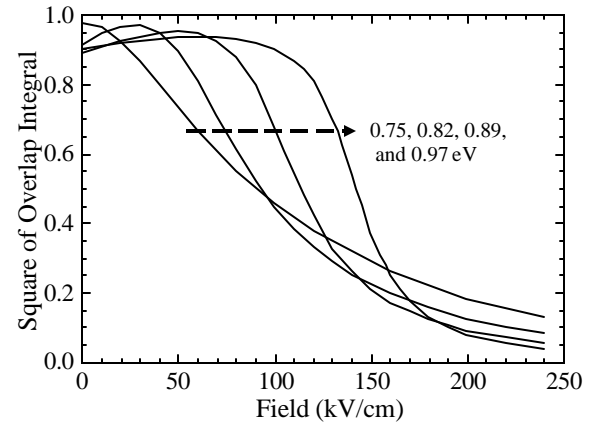


Fig. 3. The square of the overlap integral for the 10-nm thick InGa(Al)As/InAlAs IQW with increasing intra-step-barrier bandgap energy.

Similar calculations have been carried out for the 10-nm thick InGaAsP/InGaAsP IQW lattice-matched to InP. The bandgap energies of the well and the barrier are chosen to be 0.77 and 1.08 eV, and the bandgap energy for the intra-step-barrier is increased from 0.77 (no intra-step-barrier) to 0.82, 0.86, and 0.89 eV. Similar trends as the InGa(Al)As/InAlAs IQW are observed here. At an intra-step-barrier bandgap

energy of 0.89 eV, the onset of the red shift is delayed to ~ 100 kV/cm.

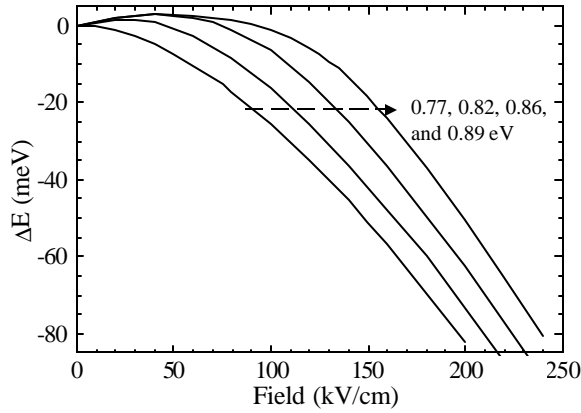


Fig. 3. The transition energy shift as a function of the applied electric field for the 10-nm thick InGaAsP/InGaAsP IQW with increasing intra-step-barrier bandgap energy.

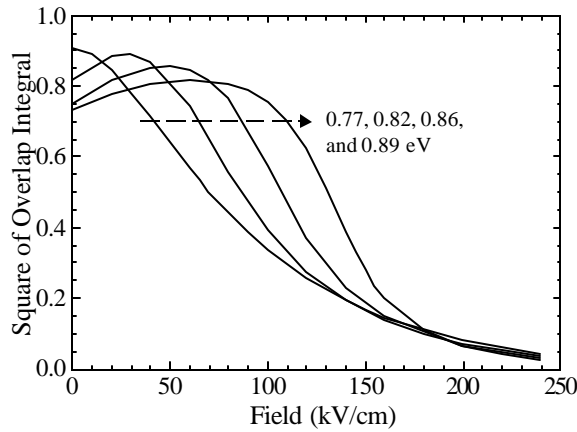


Fig. 4. The square of the overlap integral for the 10-nm thick InGaAsP/InGaAsP IQW with increasing intra-step-barrier bandgap energy.

A test IQW EAM structure based on the InGa(Al)As/InAlAs material system was grown by molecular beam epitaxy. The material structure is as follows: a semi-insulating InP substrate, a 0.5- μm n -InAlAs buffer layer ($n = 1 \times 10^{19} \text{ cm}^{-3}$), 13 periods of intrinsic IQW composed of the InAlAs (8 nm)/InGaAs (5 nm)/InGaAlAs (5 nm), an InAlAs (8 nm) barrier, a 1.2- μm p -InAlAs ($p = 2 \times 10^{17} \text{ cm}^{-3}$), and a 50-nm p -InGaAs ($p = 1 \times 10^{18} \text{ cm}^{-3}$) contact layer. The 5-nm thick quaternary InGaAlAs intra-step-barrier was substituted in the growth run by a short

superlattice consisting of 5 periods of InGaAs (0.3 nm)/InAlAs (0.7 nm) which has a nominal bandgap energy of ~ 0.97 eV.

Ring diodes for the surface-normal absorption measurement as well as waveguide EAMs were fabricated from this material. Fig. 5 shows the absorption coefficient (normalized for both the well and barrier) estimated from the transmission measurement of the ring diode. It is observed that in the bias range of 0 to 2 V, the absorption edge due to the exciton remains essentially stationary, signifying the suppression of the red shift as predicted. As the bias is further increased, the absorption edge moves toward the longer wavelengths as in the case of the conventional QCSE. The absorption in the wavelength range of 1500 – 1600 nm at zero bias is a measurement artifact caused by the absorption in material outside of the IQW layer.

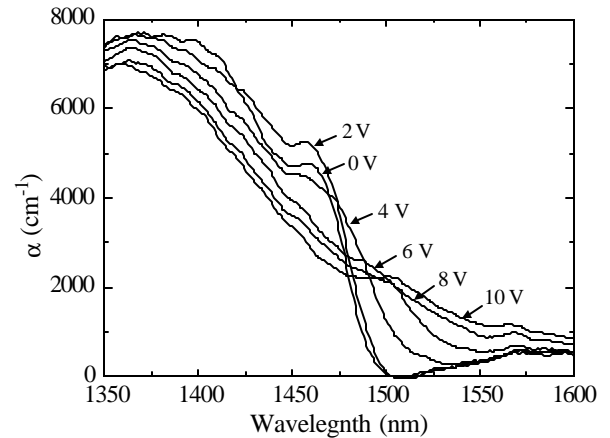


Fig. 5. Absorption coefficient of the InGa(Al)As/InAlAs IQW sample estimated from the transmission measurement on the ring diode.

The transfer curve of the waveguide EAM was measured at the laser wavelength of 1.543 μm and -3 dBm optical power. The waveguide length was 150 μm . Shown in Fig. 6 are the transmission through the EAM detected at the remote detector which has a responsivity of ~ 0.9 A/W and the modulator photocurrent as a function of the applied bias. From the transmission curve, we observe that the onset of the red shift is delayed to ~ 2.5 V. This is consistent with the

change of the absorption coefficient as a function of the bias shown in Fig. 5.

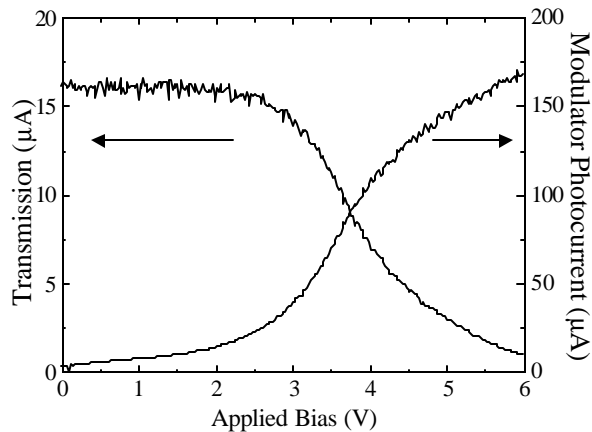


Fig. 6. Measured modulator transfer curve (transmission measured at the remote detector) and the photocurrent generated at the modulator.

In conclusion, we have demonstrated that the intra-step-barrier can suppress the red shift in the QCSE and delay its onset to a higher electric field for both the InGa(Al)As/InAlAs and InGaAsP/InGaAsP QWs. Preliminary experimental results on the InGa(Al)As /InAlAs IQWs confirm that the intra-step-barrier plays a critical role in delaying the onset of the red shift to ~ 2.5 V.

On-going efforts include characterizing the saturation optical power of this device.

Acknowledgment:

The authors like to thank Ms. Yuling Zhuang and Mr. Alan Chen at UCSD for helpful

discussions. This work is supported by a DARPA contract on RF-Lightwave Integrated Circuits (RFLICS), and the California MICRO Program (industrial sponsor: Raytheon).

References

1. S. A. Pappert, R. J. Orazi, T. T. Vu, S. C. Lin, A. R. Clawson, and P. K. L. Yu, *IEEE Photon. Technol. Lett.* **2**, 257 (1990).
2. T. H. Wood, J. Z. Pastalan, C. A. Burrus. Jr., B. C. Johnson, B. I. Miller, J. L. deMiguel, U. Koren, and M. G. Young, *Appl. Phys. Lett.* **57**, 1081 (1990).
3. F. Devaux, E. Bigan, A. Ougazzaden, F. Huet, M. Carré, and A. Carencio, *IEEE Photon. Technol. Lett.* **4**, 720, (1992).
4. A. Ougazzaden, F. Devaux, *Appl. Phys. Lett.* **69**, 4131 (1996).
5. T. H. Wood, T. Y. Chang, J. Z. Pastalan, C. A. Burrus. Jr., N. J. Sauer, B. C. Johnson, *Electron. Lett.* **27**, 257 (1991).
6. K. Wakita, I. Kotaka, S. Matsumoto, R. Iga, S. Kondo, and Y. Noguchi, *Jpn. J. Appl. Phys.* **37**, 1432 (1998).
7. R. Sahara, K. Morito, K. Sato, Y. Kotaki, H. Soda, and N. Okazaki, *IEEE Photon. Technol. Lett.* **7**, 1004 (1995).
8. K. K. Loi, I. Sakamoto, X. B. Mei, C. W. Tu, and W. S. C. Chang, *IEEE Photon. Technol. Lett.* **8**, 626 (1996).
9. D. S. Shin, P. K. L. Yu, and S. A. Pappert, *J. Appl. Phys.* **89**, 1515 (2001).